RSC Advances

PAPER

View Article Online
View Journal | View Issue

Cite this: *RSC Adv.*, 2025, **15**, 44024

Evaluating the regenerative capacity of biosynthesized nano formulated 3D scaffolds in scald burn healing

Shazmeen Aslam,[a] Tooba Jabri,[b] Maria Khalid,[b] Maaz Bin Maqsood,[a] Arshad Hasan,[c] Afeefa Shakir,[b] Saifullah*[a] and Muhammad Raza Shah[b]

Severely burned patients require effective regenerative measures to overcome barrier defects and risk of infection. The aim of the investigation was to evaluate the regenerative capacity of DPMSCs (dental pulp-derived mesenchymal stem cells) presented in the form of nanomaterial-enriched scaffolds for tissue regeneration. These injuries specifically need proper wound repair because third and fourth-degree burns cut deep into tissues. Regenerative solutions through mesenchymal stem cells appear very promising for tissue reconstitution. However, tissue engineering has a significant difficulty in improving cell survival and retention in target tissues since direct transplantation cannot achieve these outcomes due to low cell retention rates and cell redistribution into other organs. Therefore, the study focuses on recent advances in developing injectable hydrogels, designed to address these limitations as a three-dimensional cell culturing matrix with increased water absorption capacity *in vivo*. The hydrogel offers an environment that is conducive to cell adhesion and growth, which is not achieved by the stem cells and nanoparticles itself, since the nanoparticles significantly contributes to promote only biological properties. We reported a new nanocomposite hydrogel of chitosan (CHI), poly(*N*-isopropylacrylamide) (PNIPAm) with zinc oxide nanoparticles (ZnO). Physicochemical characterisation demonstrated successful ZnO incorporation, increased structural strength, improved thermal stability, decreased swelling and increased water retention. The *in vitro* results showed that the isolated cells expressed CD44, CD90 and CD105 positive surface markers of MSCs (mesenchymal stem cells) as well as the capacity of trilineage differentiation. Cytotoxicity studies showed concentration dependent viability for blank hydrogel, whereas, honey-ZnO nanocomposite hydrogel showed significantly high cell survival indicating improved biocompatibility. *In vivo* tests using a rat scald burn model demonstrated efficient/improved/increased wound healing in the hydrogel treated groups, in particular, when it was associated with dental pulp stem cells (DPMSCs). The analysis of the gene expression profile showed that the treatment with DPMSCs resulted in the significant reduction of several inflammatory cytokines and the elevation of TGF-β (transforming growth factor-β) and COL-1 (collagenase-1), that are possible markers of regeneration. Hypermetabolic response profiling demonstrated that the hydrogels incorporated with DPMSCs, particularly containing honey, were able to suppress systemic hypermetabolism through regulation of corticosterone levels. In summary, the honey-ZnO nanocomposite thermoresponsive hydrogel fusion with DPMSCs has good prospects for deep burn wound treatment due to its enhanced biocompatibility and amplified regeneration properties.

Received 29th August 2025
Accepted 22nd October 2025

DOI: 10.1039/d5ra06471f

rsc.li/rsc-advances

1 Introduction

The skin is the body's primary epithelial barrier, providing defense against infection, environmental stress, and physical injury. If this critical barrier is breached, it offers a direct route for microbes (to enter) the body; at localized levels of the skin or even in other organ systems. The natural course of skin wound healing consists of a series of overlapping phases. Immune cells such as neutrophils and macrophages are initially attracted to bail out the debris at the wound site. Then growth factors and interleukins are released into the area, which in turn draw in other immune

[a]*Department of Biotechnology, University of Karachi, Karachi, Pakistan. E-mail: shazmeenaslam1@gmail.com; maazmaqsood1997@gmail.com; saifullah@uok.edu.pk*

[b]*HEJ Research Institute of Chemistry, International Center for Chemical and Biological Sciences, University of Karachi, Karachi, 75270, Pakistan. E-mail: toobaasif137@gmail.com; mari.talha@gmail.com; afeefashakir2001@gmail.com; raza.shah@iccs.edu*

[c]*Dow Dental College, Dow University of Health Sciences, Baba-e-Urdu Road, Karachi, Pakistan. E-mail: arshad.hasan@duhs.edu.pk*

system components for reparative action. Subsequently, the fibroblasts proliferate and collagen deposition take place to develop extracellular matrix. Finally, the repair phase is followed by fibroblasts transforming themselves into myofibroblasts, that are essential components in compressing connective tissue and to bridge the gap left during wound impairment.[1]

Burn injury is among the most debilitating traumas to inflict humans. According to the World Health Organization, each year about 300 000 deaths occur worldwide due to burns.[2] Burn injury induces numerous organ dysfunctions resulting in high levels of morbidity and mortality.[3–5] Among these, thermal burns are the prevalent and, often times, result in devastating injury that can lead to prolonged suffering and substantial morbidity. Based on thermodynamic principles one can hypothesize that scald burns would cause more severe injuries than contact burns because of water's higher thermal effusivity.[6] Moreover, a hallmark of burn injury is a hypermetabolic response that results in significant pathological alterations in a number of tissues. Particularly, burns of large surface area manifest into systemic problems like hypermetabolism and sepsis.[4,5,7] The primary goal of this response is to provide sufficient energy for maintaining organ function and homeostasis under demanding trauma conditions. Prolonged hypermetabolism becomes detrimental and is associated with widespread catabolism, multi-organ failure, and death.[8] Recent advances in wound care technology have decreased the burn-injury induced mortality but the therapeutic methods to treat severe burns are still limited and expensive. Therefore, considering all these factors, the resources required to care for burn patients creates an enormous burden on the health care system.

Stem cells alone can regenerate skin elements that are absent in standard tissue-engineered skins.[9] Prominently, mesenchymal stem cells (MSCs) are a group of multipotent adult stem cells that possess unique adherent, fibroblast-like morphology and *trans*-differentiation capabilities into osteogenic, adipogenic, and chondrogenic lineages.[10] Moreover, MSCs can be engineered to secrete or drive small molecules that are involved in important paracrine events such as signaling for cell survival and angiogenesis and are also responsible for the removal of necrotic cells, wound contraction, diminishing scar formation by releasing immunosuppressive factors that promotes re-epithelization.[11,12] Therefore, stem cells were considered as the key players in this study which accelerates wound healing, if further combined with factors that increases its cell survival and microenvironment. The skin regeneration varies upon the wound's microenvironment. The prolonged release of therapeutic molecules from grafted stem cells is considered an important approach to treat multiple diseases.[13] To address this issue, nanoparticles and hydrogels have been strongly pursued as stem cell delivery carriers that can replicate features of the tissue environment and control the proliferation and differentiation of stem cells,[14] which is hypothesized in this study, using injectable hydrogel encapsulated with nanoparticles and stem cells which increases the cell survival and migration to the wound site and the prolong release of nanoparticles will maintain the wound microenvironment reducing inflammation. Hydrogels are 3D crosslinked conformations of hydrophilic natural (*e.g.*, proteins, polysaccharides) or synthetic (*e.g.*, polyethylene glycol) polymers with a high water content that do not dissolve. They offer critical biological and physical support, preserving the encapsulated stem cells, and porous matrix allows ions to transport through favorably, providing nutrient perfusion and waste exchange to encapsulated cells.[15] Additionally, hydrogels can be engineered with cell-interactive substances to enhance cell viability and to selectively inhibit stem cell differentiation, which will have great potential in the autologous stem cell-based therapies for desired tissue regeneration.[16,17]

The use of nanotechnology has increased enormously as it has shown to offer promising strategies to improve the treatment of numerous disorders, including burns and wounds. Nanoparticles are small particles that range in size from 1–100 nm which confers an advantage over micro-sized particles owing to their unique small size, large surface area, and large surface-to-volume ratio in terms of rate of activity.[18,19] The green synthesis of nanoparticles has gained attention as being nontoxic, safe for humans, eco-friendly, and economically viable, compared to its chemical and physical synthesis.[20] Therefore, another important goal was to synthesis nanoparticles that are nontoxic and promote wound healing by preventing oxidation in the tissue environment. In this context, zinc oxide (ZnO) was selected for its well-documented antimicrobial, antioxidant, and wound-healing activities, while honey was employed as a natural reducing and stabilizing agent owing to its rich composition of flavonoids, phenolic acids, and sugars that can mediate nanoparticle formation. The rationale was to combine the intrinsic antimicrobial potential of ZnO with the long-known therapeutic and regenerative effects of honey to create a biocompatible nanocomposite system suitable for tissue engineering and burn wound healing. Nanomaterials have unique advantages in controlling stem cell function and in tissue regeneration due to their biomimetic characteristics and special biological and mechanical properties.[21] The scaffolds can be in the form of nanofibrous materials, or polymeric nanoparticles in the form of hydrogels, which offers certain advantages over the ones used for drug delivery due to its biodegradability, biocompatibility, low immunogenicity, and low toxicity.[22–24] Therefore, in this study we investigated the therapeutic potential of the combinational therapy of biosynthesized nanoparticles from honey extract, and dental pulp derived mesenchymal stem cells (DPMSCs) using a 3D scaffold in the form of hydrogel to treat the full thickness scald burn in rat model. The study targeted the recent advances in tissue engineering in terms of nanobiotechnology and stem cells as novel treatment strategy for burns.

2 Material and methods

2.1 Materials

Nisopropylacrylamide (NIPAm), chitosan, glutaraldehyde and ammonium persulfate (APS), were purchased from Sigma-Aldrich, absolute ethanol was purchased from Merck Germany. Deionized and distilled water used was prepared in-house.

2.2 Methodology

2.2.1 Green synthesis of HZnO nanoparticles. HZnO nanoparticles were synthesized using zinc acetate dihydrate

$[Zn(OAc)_2 \cdot 2H_2O]$ as a precursor *via* an autocombustion method. A 0.3 M solution of $Zn(OAc)_2 \cdot 2H_2O$ (50 mL) was prepared, to which 2 mL of honey was added. The mixture was stirred at 500 rpm for 2 hours at 60 °C, resulting in the transformation of the original yellow precursor solution into a gummy brownish gel. This gel was then heated at 100 °C for 1 hour, followed by annealing at 600 °C. The resulting product was crushed to obtain a dark brown crystalline powder of HZnO nanoparticles, which were subsequently subjected to characterization. This mild synthesis approach deliberately preserves the honey capping, maintaining its organic functional groups and therapeutic properties.

2.2.2 Synthesis of CHI-PNIPAm and CHI-PNIPAm-HZnO thermoresponsive hydrogels. Thermoresponsive CHI-PNIPAm hydrogels were synthesized *via* free radical polymerization. The feed ratios of the polymer and free radical initiator are presented in Table 1. Chitosan (CHI) was dissolved in a 0.1% (v/v) aqueous acetic acid solution under continuous stirring. Separately, *N*-isopropylacrylamide (NIPAm) and ammonium persulfate (APS, 1% w/w of the total polymer feed) were dissolved in water and added to the CHI solution, maintaining the total volume below 10 mL. The reaction mixture was stirred at room temperature overnight.

Following the completion of the grafting reaction overnight, glutaraldehyde was added to initiate crosslinking. Glutaraldehyde (1.3–2.4% w/w of total polymer weight) was added dropwise to the mixture and stirred for 2 hours to complete the crosslinking reaction. The resulting hydrogel solution was transferred into labeled tubes and placed in a water bath at 25 °C. Gelation was monitored by gradually increasing the bath temperature to 37 °C. Gelation time and gelation temperature were recorded for each formulation to determine the optimal composition. Gel fraction was also calculated.

To minimize interference with the thermoresponsive gelation process, nanoparticles were incorporated following polymerization and crosslinking a strategy previously shown effective in polysaccharide-based nanocomposite dressings.[25] The optimized hydrogel formulation was equilibrated below 20 °C prior to the addition of honey-mediated ZnO nanoparticles (HZnO, 0.5% w/v). The mixture was stirred for 2 hours to obtain a homogeneous CHI-PNIPAm-HZnO nanocomposite hydrogel. This composite hydrogel was then evaluated for gelation temperature, gelation time, and gel fraction using the same protocol as for the blank hydrogel.[26]

Table 1 Polymer feed ratios, initiator (APS) concentration, and glutaraldehyde content used in the formulation of thermoresponsive hydrogels

Formulation	Polymer feed ratio (CHI : NIPAm) mg 10 mL^{-1}	APS (mg) 10 mL^{-1}	Glutaraldehyde μL 10 mL^{-1}
1	20 : 140	1.6	4
2	20 : 140	1.6	6
3	20 : 140	1.6	8
4	20 : 160	1.8	4.5
5	20 : 160	1.8	6.5
6	20 : 160	1.8	8.5
7	20 : 180	2.0	5
8	20 : 180	2.0	7
9	20 : 180	2.0	9
10	20 : 200	2.2	5.5
11	20 : 200	2.2	7.5
12	20 : 200	2.2	9.5
13	20 : 220	2.4	6
14	20 : 220	2.4	8
15	20 : 220	2.4	10

2.2.3 Sol–gel–sol phase transition temperature measurement ($T_{sol-gel}$) and measurement of gelation time. Phase transitions of the polymer solutions were evaluated using visual inspection techniques. Each formulation was transferred into a glass vial and placed in a temperature-controlled water bath. The temperature was gradually increased from 25 °C to 37 °C, and the sol–gel transition temperature ($T_{sol-gel}$) was identified as the point at which initial turbidity appeared. To determine the transition to a non-flowing gel state, the vial was gently tilted; the absence of flow indicated successful gelation.

Gelation time at physiological temperature was determined by placing approximately 1 cm of each formulation into test tubes immersed in a water bath maintained at 37–38 °C. The time required for the solution to form a stable gel was recorded, based on observable changes such as turbidity, loss of fluidity, or the development of a self-supporting structure in clear systems. Formulations that failed to exhibit gelation evidenced by the absence of turbidity or significant viscosity increase were noted for comparative evaluation.

2.2.4 Sol–gel fraction. To quantify the soluble (sol) and insoluble (gel) components in stabilized hydrogels, a sol–gel fraction analysis was performed. Only hydrogel formulations that achieved a stable, non-flowable state were chosen for this analysis. These stable gels were minced into smaller pieces (7–9 mm). The cut hydrogel pieces underwent drying in a vacuum oven at 38 °C for 24 hours, followed by a week-long storage in an incubator to guarantee weight stabilization. The dried hydrogel samples were then accurately weighed to obtain the initial dry weight (W_i). To remove the sol fraction, the dried hydrogel pieces were submerged in water at 50 °C for 6 hours. After the extraction process, the hydrogel pieces were air-dried at room temperature for 24 hours and then completely dried in an incubator at 38 °C.

The following formulas were used to calculate the sol and gel fractions of the hydrogels gel fraction (%) $= W_f/W_i \times 100$

$$\text{Sol fraction (\%)} = 100 - \text{gel fraction}$$

where, W_f is the weight of the dried hydrogel after sol extraction and drying and W_i is the initial dried weight of the hydrogel before sol extraction.

2.2.5 Line spread test (LST). The spreadability of the thermoresponsive preparation was evaluated by the LST method. A cylindrical chamber (3 cm height, 1.0 cm diameter, placed on a Petri dish with concentric circles) was saturated at either 20 or 37 °C 1 min. The tube was then charged with 1.5 mL of the gel and immediately withdrawn, allowing the gel to expand for 30 seconds. The average spread distance was extracted by taking

the average of the distances between the centers of the four quadrants of the spread.

2.2.6 Swelling behavior. Swelling behavior was measured by the method described in a previous study. Swelling studies were performed by allowing 25 mg of lyophilized copolymer to swell in 5 mL PBS (pH 4 and 7.4) at 4 °C for 24 h, followed by solidification at 37 °C for 1 h. The weight of the swollen hydrogels was then measured at pre-determined time points after carefully removing excess PBS.

The equilibrium swelling ratio was calculated according to the following equation:

$$\text{Swelling ratio}(\%) = \frac{W_t - W_o}{W_o} \times 100$$

where W_o and W_t respectively represent the weight of initial lyophilized copolymer and the weight of swollen hydrogel disc.

2.2.7 Scanning electron microscopy. Scanning electron microscopy was employed to analyze the surface morphology of both the optimized blank CHI-PNIPAm hydrogel and the CHI-PNIPAm-HZnO nanocomposite thermoresponsive hydrogel. Lyophilized hydrogel samples were affixed to metallic stubs, sputter-coated with gold, and then examined using a JEOL-JSM-6380A scanning electron microscope.

2.2.8 X-ray diffraction. The crystalline structure of dried hydrogel discs was investigated *via* X-ray diffraction using a PANalytical X'Pert multipurpose diffractometer, employing Cu Kα radiation. Data were acquired over a 2θ range of 10–80°.

2.2.9 Thermogravimetric analysis. To determine the thermal stability, thermogravimetric analysis was performed. Samples were analyzed using a Shimadzu TGA-50 micro-thermogravimetric analyzer, heating from room temperature to 600 °C at 15°C min^{-1} under a nitrogen (N_2) atmosphere.

2.2.10 Fourier transformed infrared spectroscopy. Infrared spectroscopy was used to investigate the chemical interactions within the CHI-PNIPAm and CHI-PNIPAm-HZnO samples. Dry samples were analyzed using an attenuated total reflectance spectrophotometer, with spectra collected in the range of 600–4000 cm^{-1}. Samples were placed on a ZnSe plate and analyzed at room temperature.

2.2.11 Injectability analysis. To assess injectability, the force needed to push the formulation through 22G and 23G needles at flow rates of 1.0 and 2.0 mL min^{-1} was measured using a manual spring balance.

2.2.12 Isolation and propagation of human dental pulp derived mesenchymal stem cells (DPMSCs). All human participation was voluntary and after informed consent. It followed Helsinki declaration for the participation of human subjects in medical research and after the approval of the Ethical Review Board (IRB-2516) of the Dow University of Health Sciences. Human premolars or wisdom teeth from healthy adolescents and young adults (16–25 years old) were harvested. The teeth were sterilized by 70% ethanol and two washing steps with PBS in a Petri dish were performed in order to remove tissue debris and periodontal ligament. Samples were prepared using a sterilized dental disc and the pulp chamber was opened with a chisel/mallet, thus avoiding thermal damage to the tissue. The pulp tissue was then removed and immediately transferred to Petri dishes with complete DMEM (Gibco, USA; 11995-065) media supplemented with 10% FBS (Biowest, USA; S1810-500), 100 U penicillin/streptomycin (Gibco, USA; 15140) and 1 mM sodium pyruvate (Gibco, USA; 30183). The tissue was minced into small fragments of 1–2mm using scalpel blade and transferred to a T-25 cell culture flask, incubated at 37 °C in 5% CO_2 as shown in Fig. 1. The cells were propagated through a standardized culture method (Aslam, 2020). For subsequent passaging (P1 through P6), cells were subcultured upon achieving approximately 80% confluency. Subcultured cells were trypsinized for around 3 min, and the cell detachment was directly observed using a phase-contrast microscope (TE 2000S, Eclipse, Nikon, Japan). The cell suspension was centrifuged at 1000 rpm for 8 min (Centrifuge 5804R, Eppendorf, Germany) to create a cell pellet. This pellet was then resuspended in new DMEM, transferred to a T-75 culture flask with 10–12 mL of complete DMEM and allowed to grow under the appropriate

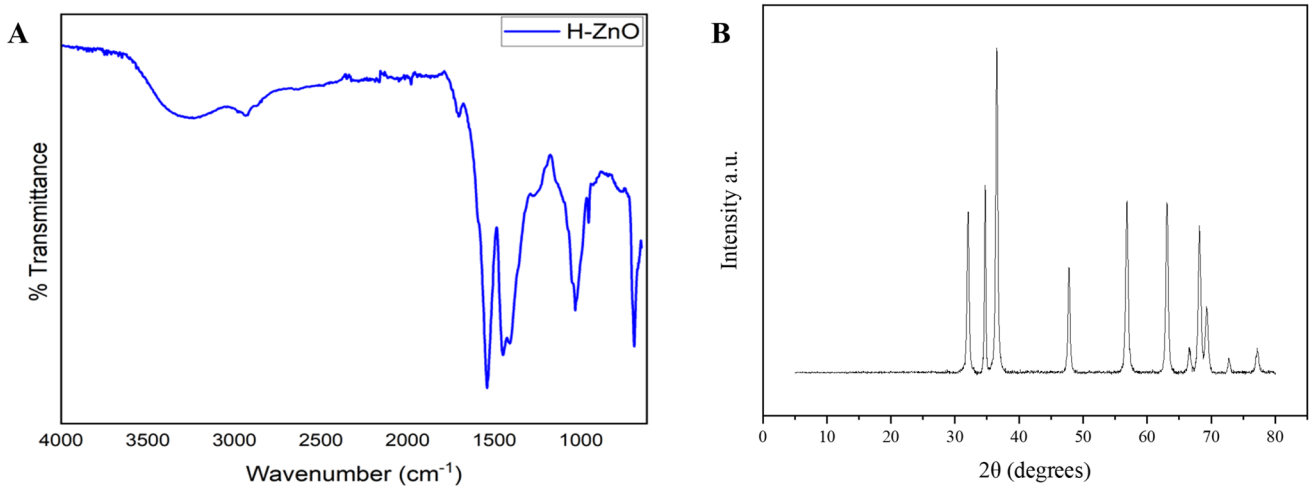

Fig. 1 (A) FTIR spectra and (B) X-ray diffractogram of HZnO.

Table 2 Experimental Groups

S. no	Groups	Abbreviations
1	Burn control	BC
2	DPMSCs	DPMSCs
3	Honey zinc oxide hydrogel	CHI-PNIPAm-HZnO or (HH)
4	Honey zinc oxide hydrogel + DPMSCs	CHI-PNIPAm-HZnO + DPMSCs (HHSC)
5	Blank hydrogel	CHI-PNIPAm (BH)
6	Blank hydrogel + DPMSCs	CHI-PNIPAm + DPMSCs (BHSC)

CO_2 atmosphere. Cell adhesion and proliferation were monitored microscopically on alternate days.[27]

2.2.13 Immunophenotyping. The cells of passage 3 (around 250 000 cells per tube) were incubated with CD44, CD90, CD105 and CD45 anti-human antibodies with their isotypes for 30 min at 4 °C. The antibody concentration was applied according to the manufacturer's protocol (Thermofisher scientific, US). The cells were then analyzed for surface markers (antibodies) by immunocytochemistry. All the samples were run in triplicates, and unlabeled cells containing only DAPI (MP Biomedical Inc, USA; 157574) were taken as control.[13]

2.2.14 Trilineage differentiation. The trilineage differentiation potential of DPMSCs was assessed for chondrogenic, osteogenic, and adipogenic lineages. Approximately 4 × 104 Passage 3 DPMSCs were seeded per well in 6-well plates and allowed to reach 60–70% confluency before induction. Cells were cultured in specific chondrogenic (StemPro™ Chondrogenesis Differentiation Kit, Thermoscientific: A1007101) osteogenic (StemPro™ Osteogenesis Differentiation Kit, Thermoscientific; A1007201), or adipogenic (StemPro™ Adipogenesis Differentiation Kit, Thermoscientific; A1007001) differentiation media, with media changes every 3–4 days for a total of 21 days. Post-induction, osteogenic differentiation was characterized by alizarin red (Sigma Aldrich; A5533) staining for calcium deposits, chondrogenic differentiation by alcian blue (Sigma Aldrich; A9186) staining for proteoglycans, and adipogenic differentiation by oil red O (Sigma Aldrich; O0625) staining for lipid droplets, counterstained with hematoxylin. All stained cultures were then analyzed and imaged using an inverted microscope at 4× and 10× magnification.[13]

2.2.15 Cytotoxicity analysis of thermoresponsive hydrogel (MTT assay). Cells were obtained by trypsinization at passage 3 and 96 well plate was prepared by seeding 5×10^3 cells per well, incubated for 1–2 days in a CO_2 (5%) incubator (Heracell 160i, Thermoscientific, US). Once 80% confluency is attained, the cells were then treated with different concentrations taken in (300, 500, 700, 1000, and 5000) μg mL^{-1} of all the treatment groups in triplicate and a serum-free control in a serum-free media (Gibco, USA 11995–065). The plate was then incubated for 24 h in a CO_2 incubator. The treatment was then removed followed by the addition of 100 μL of working MTT (Sigma, USA; M5655) dye (0.5 mg mL^{-1}), kept under 3 h of incubation at 37 °C. The dye was then decanted gently followed by the addition of 200 μL of DMSO (Sigma, USA; D8418), producing purple color. The plate was then analyzed in the spectrophotometer (Multiskan FC microplate photometer, Thermo Scientific, US) by measuring absorbance at 570 nm (Table 2).

2.2.16 Third degree burn wound animal model. Male Wistar rats (6–8 weeks old) were acclimatized for two weeks under ethical guidelines (IBC KU-437/2024). Anesthesia was induced *via* intraperitoneal ketamine (Randlab, Australia) (60 mg kg^{-1}) and xylazine (Randlab Xylazine™ 100 injection, Australia) (7 mg kg^{-1}). The dorsal and ventral areas were shaved, and a full-thickness burn covering 60% total body surface area (30% each side) was created by immersing skin in 98 °C water for 10 seconds using a heat-resistant mold. Post-burn, animals received subcutaneous antibiotics (penicillin/streptomycin: 150 000 IU kg^{-1}; Gibco, USA: 15140) and analgesics (Diclofenac Sodium: 0.03 mg kg^{-1}, DYCLO; Indus Pharma Pvt. Ltd), followed by daily monitoring for recovery, pain, or infection (SI Fig. S1).[6]

2.2.17 Transplantation of DPMSCs & hydrogel. The cells were prepared for transplantation by harvesting using the method of trypsinization. The cell pellet was suspended in 1 mL PBS and manual cell count was performed using a Neubauer chamber with the aid of 0.4% trypan blue (MP Biomedicals Inc; 195332) used in a ratio of 1 : 1. After the cell count 1 million cells were collected and washed twice with PBS by centrifugation at 8000×*g* for 10 min to remove all the traces of media before transplantation. The cell pellet obtained was then collected in cold PBS for transplantation. The rats were anesthetized and 1 mL of the cells were transplanted using insulin syringe in the periphery of the burn wound at multiple sites covering the entire wound area on the dorsal and ventral side after 72 h of burn infliction.

Similarly, 1 mL of the hydrogels, CHI-PNIPAm and CHI-PNIPAm-HZnO were transplanted using insulin syringe at the burn wound periphery at multiple sites covering the entire wound area on the dorsal and ventral side. Additionally, for the CHI-PNIPAm-HZnO + DPMSCs and CHI-PNIPAm + DPMSCs the harvested cells were seeded in the injectable hydrogels to develop a 3D scaffold for transplantation. The stem cells loaded hydrogels were then transplanted in a similar way as DPMSCs and hydrogel.[13]

2.2.18 Macroscopic visualization of burn. The macroscopic visualization was performed on the control and treated burn wounds at week 1 and week 2 for analyzing their rate of healing and scab detachment. Further, the burn area was also visualized for signs of angiogenesis at the time of tissue harvest for sample collection. The images were captured at defined time points of

Table 3 List of primers of wound released cytokine genes

S. no.	Genes	Primer sequence (5′-3′)
1	Interleukin 1 beta (IL-1β)	Forward: TCATCTTTGAAGAAGAGCCCGT reverse: GTTCTGTCCATTGAGGTGGAGA
2	Interleukin 6 (IL-6)	Forward: GATGGATGCTTCCAAACTGGATA reverse: TGAATGACTCTGGCTTTGTCTTT
3	Transforming growth factor (TGF-β)	Forward: TCGCCAGTCCCCCGA reverse: TCGGGCTCCGGGTCA
4	Vascular endothelial growth factor A (VEGF)	Forward: CCAATTGAGACCCTGGTGGA reverse: TCCTATGTGCTGGCTTTGGT
5	Collagenase-I (COL I)	Forward: ACAAAACCACCAAGACCTCC reverse: GTTGGTCTGTTTCCAGGGTT
6	BCL2 associated X, apoptosis regulator (bax)	Forward: CTTCTTCCGTGTGGCAGC reverse: CAGACAAACAGCCGCTCC
7	Matrix metallopeptidase 9 (MMP-9)	Forward: TACCAGCTACTCGAACCAATCA reverse: AAATAAAAGGGCCGGTAAGGTG

day 1, day 4, day 7, and day 14 in control burn to validate the burn wound model and at week 1 and week 2 post treatment in all the treatment groups for evaluation of gradual progression of burn healing.

2.2.19 Histopathological analysis. The tissue samples were obtained from the experimental animals and processed at the Histopathology Department at Dow University of Health Sciences. Briefly, the tissue samples were fixed in 10% formalin and dehydrated in increasing concentrations of ethanol (ThermoFisher Scientific; 64-17-5), embedded in paraffin wax. Tissues were sectioned at 6 μm thick slices using a microtome and mounted on glass slides followed by hematoxylin (Carl Roth, USA; T.864.1) and eosin (Carl Roth, Germany; X883.1) (H&E) staining, dehydration and mounting. Samples were then subsequently visualized using a light microscope (Nikon, Japan) at 10× magnification.

2.2.20 Gene expression analysis (Table 3). For molecular analysis, nuclease-free consumables and surfaces were maintained. Burn wound tissue samples (90–100 mg) from both treated and control groups were homogenized in 1 mL of one-step RNA reagent (BS410A, Bio Basic, Canada), followed by chloroform extraction and centrifugation. The RNA-containing aqueous phase was then precipitated with 100% isopropanol and washed twice with ethanol before reconstitution in nuclease-free water and storage at −80 °C. RNA quantification and purity assessment (260/280 nm ratio) were performed using a NanoDrop 2000 spectrophotometer (Thermo Scientific, USA), and total yield was calculated. Subsequently, 1 μg of the extracted RNA was reverse-transcribed into complementary DNA (cDNA) using the RevertAid first strand cDNA synthesis kit (K1621, Fermentas, ThermoFisher Scientific, USA) following manufacturer guidelines. Primers for target wound healing genes were designed *via* NCBI Primer-Blast, acquired from BioBasic (Canada), and reconstituted in Tris–EDTA buffer (Invitrogen, USA; 15400–054). Finally, gene expression was quantified by quantitative real-time PCR (qRT-PCR) on QuantStudio 7 flex (Applied biosystems, USA), utilizing SYBR green master mix (Thermoscientific; K0221), cDNA, and specific primers, with GAPDH as an internal control. All reactions were performed in triplicates, and fold changes were determined using the $2^{-}(\Delta\Delta C_t)$ method.[13]

2.2.21 Evaluation of hypermetabolic response. The hypermetabolic response was evaluated by analysis of corticosterone and TNF-α concentration in burn tissue samples using ELISA kit (cat#EIACORT: corticosterone competitive ELISA kit). Protein was isolated from 100 mg of control and treated burn tissue samples by homogenization in 1 mL of cell lysis buffer containing 10 μL of protease inhibitor cocktail. Following centrifugation at 12 000×*g* (4 °C) for 20 minutes, the supernatant was collected and stored at −80 °C. Protein expression analysis was subsequently performed in triplicates *via* ELISA, strictly adhering to manufacturer's protocols. Briefly, standards were prepared, and samples (1 : 10 diluted) were added to wells alongside specific conjugates and antibodies for target analytes, such as corticosterone (1 h RT incubation). Plates were thoroughly washed, incubated with TMB substrate, stopped with stop solution, and absorbance was measured at 450 nm.[28]

2.2.22 Statistical analysis. Every data set was statistically analysed using IBM SPSS Statistics 21. Descriptive statistics, namely one-way ANOVA with *post hoc* Bonferroni test was used for analysis. There were three observations (n); all results were shown as mean ± SEM; the degree of confidence was set at $p \leq 0.05$ (* = $p < 0.05$, ** = $p < 0.01$ and *** = $p < 0.001$).

3 Result and discussion

3.1 Synthesis and characterization of HZnO nanoparticles

HZnO nanoparticles were synthesized using bee honey as a bioreductant, which also acts as a stabilizing and capping agent.[29] The structural and chemical features of the synthesized HZnO nanoparticles were analyzed using Fourier-transform infrared spectroscopy (FTIR) and X-ray diffraction (XRD). The FTIR spectrum, shown in Fig. 1A, revealed distinct absorption bands indicative of organic functional groups derived from honey, which acted as a natural reducing and stabilizing agent during synthesis. A broad peak near 3000 cm^{-1} was attributed to O–H stretching vibrations, commonly associated with alcohols, phenols, water molecules, and organic acids present in honey. A relatively small band around 1700 cm^{-1} indicated the presence of carbonyl (C=O) functionalities, potentially originating from gluconic acid, while a signal at approximately 1600 cm^{-1} was linked to N–H bending, characteristic of amine groups. Bands near 1400 cm^{-1} were attributed to C–O–H bending vibrations of carbohydrates, with minor contributions from C–N stretching of trace proteins. The 1100–1000 cm^{-1} region showed vibrations characteristic of C–O stretching in alcohols, esters, and

carbohydrate moieties. These features collectively confirm the involvement of honey constituents in the biofabrication of ZnO nanoparticles, playing crucial roles in reduction, capping, and long-term colloidal stability. Since our approach aimed to retain the therapeutic benefits of honey, we deliberately preserved the honey capping on the nanoparticles. Consequently, the FTIR spectrum clearly shows these organic functional groups, in contrast to literature reports where high-temperature auto-combustion or annealing often degrade honey components, resulting in flattened spectra.[30] Importantly, despite preserving these honey signatures, the crystallinity of ZnO was maintained. The XRD pattern (Fig. 1B) displayed the reflection from (100), (002), (101), (102), (103), (200), (201), (004) and (202)corresponding to the peaks obtained at 2θ values of 32.07°, 34.46°, 36.53°, 47.79°, 63.10°, 67.07°, 69.77°, 72.67° and 77.63°, respectively.[31] The observed XRD data aligns with the ZnO standard data's hexagonal wurtzite structure (JCPDS 01-080-0074) and also with the honey synthesized nanoparticles reported in literature.[30] The morphological features and size of the honey zinc oxide (HZnO) particles are clearly visible after their incorporation into the thermoresponsive gel, showing particles ranging from cuboid to spherical shapes with sizes in the nanometer range.

3.2 Synthesis and optimization of blank (CHI-PNIPAm) and nanocomposite (CHI-PNIPAm-HZnO) thermoresponsive hydrogel

Thermoresponsive hydrogels were synthesized by grafting poly(*N*-isopropylacrylamide) (PNIPAm) onto chitosan to produce a temperature-sensitive copolymer (PNIPAm-g-CHI). This was achieved *via* a "grafting-from" strategy, in which NIPAm monomers polymerize *in situ* and covalently attach to initiator sites along the chitosan backbone.[32] Unmodified PNIPAm exhibits a lower critical solution temperature (LCST) of approximately 32 °C below which it remains hydrophilic and water-soluble.[33] Above the LCST, entropy-driven hydrophobic interactions—primarily due to isopropyl groups—become dominant, leading to polymer chain collapse and gel formation.[34,35] Grafting PNIPAm onto chitosan alters the hydrophilic–lipophilic balance, resulting in a copolymer with a modified LCST.[36] The presence of polar functional groups and increased charge density in chitosan, particularly under acidic conditions, enhances polymer–water interactions and raises the LCST, as greater thermal energy is required to overcome these interactions and induce gelation.

The self-organization of hydrophilic and hydrophobic segments of a thermoresponsive polymer can assume a variety of morphologies such as a self-organized micelle, a gel, a coil, a globule, or a two-phase system, depending on the conditions.[37,38] For our intended application, the target properties include rapid and stable gelation near physiological temperature, high shape adaptability to wound geometry, strong thermoresponsiveness, and a high gel fraction.[39] To achieve these performance characteristics, we systematically varied the NIPAm-to-chitosan weight ratios (1 : 7, 1 : 8, 1 : 9, 1 : 10, and 1 : 11). Ammonium persulfate (APS) as initiator was added (1% w/w of the total polymer). Although the PNIPAm-g-chitosan copolymers was further crosslinked with glutaraldehyde (1.3–2.4% w/w with respect to the total polymer weight) to enhance its thermal and mechanical properties. Gelation was evaluated by the test tube inversion test, whereby a passing product held its form on inversion. These hydrogels also demonstrated reversible thermoresponsiveness, returning to the sol state when cooled approximately 5 °C below their LCST—behavior consistent with previously reported systems.[35,40]

3.3 Effect of crosslinker concentration on gelation behavior

The concentration of glutaraldehyde significantly influenced the gelation mechanism. At high concentrations (>2%), gelation occurred immediately upon addition due to excessive crosslinking, overriding thermoresponsive behavior. These formulations (*e.g.*, 3, 6, 9, 12, 15) formed gels through chemical means alone, as viscosity increased spontaneously before temperature-induced phase transition could occur. At the other extreme, low glutaraldehyde concentrations (<1.3%) failed to produce stable gels (*e.g.*, 1, 4, 7, 10, 13). These samples remained turbid or cloudy, showing only partial hydrophobic collapse without sufficient crosslinking to achieve structural integrity. Intermediate concentrations (1.7–1.9%) yielded the desired thermoresponsive gelation, with formulations 2, 5, 8, 11, and 14 transitioning from liquid to gel between 33–35 °C and stabilizing at 37 °C. Gelation onset and duration were influenced by the NIPAm-to-CHI ratio, where higher NIPAm content led to faster and earlier gelation.

3.4 Gelation onset, duration and gel fraction

As previously noted, formulations containing intermediate concentrations of glutaraldehyde (approximately 1.7–1.9% w/w relative to the total polymer feed) demonstrated thermoresponsive gelation, with hydrophobic collapse initiating between 33–35 °C. This behavior suggests that grafting PNIPAm onto chitosan increased the overall hydrophilicity of the copolymer system. However, as shown in Table 4, the LCST decreased with increasing NIPAm content in the feed ratio. This inverse relationship can be attributed to the fundamental role of hydrophobic interactions in PNIPAm-g-chitosan gelation. These interactions, predominantly driven by the PNIPAm segments, are entropy-dependent and become increasingly dominant at elevated temperatures due to enhanced molecular mobility. The

Table 4 Gelation onset temperature, gelation duration and gel fraction of 3 mL pre-gel assessed in test tube. Data are presented as mean ± standard deviation (S.D.)

Formulation	Gelation onset temperature (°C)	Gelation duration at physiological temperature (s)	Gel fraction (%)
2	34.2 ± 0.2	279 ± 5	80.1 ± 1
5	34.0 ± 0.1	245 ± 10	81.9 ± 2
8	33.7 ± 0.2	224 ± 10	83.3 ± 1
11	32.9 ± 0.1	190 ± 5	84.2 ± 1
14	32.5 ± 0.1	183 ± 10	85.9 ± 2

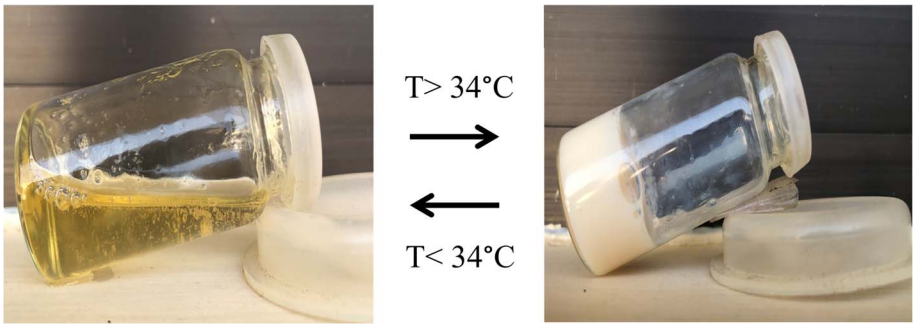

Fig. 2 Sol–gel phase transition of CHI-PNIPAm-11.

intensity of these hydrophobic forces is directly influenced by the proportion of hydrophobic content in the formulation. Higher NIPAm content results in a greater PNIPAm-to-chitosan ratio, strengthening hydrophobic interactions and enabling gelation at a lower temperature by overcoming hydrophilic forces more readily. In contrast, formulations with lower NIPAm ratios contain a larger fraction of hydrophilic chitosan, which reinforces water–polymer interactions, thereby raising the LCST and delaying gelation.

Among the tested formulations, the sample with an initial gelation onset at 33 °C exhibited the most rapid transition to a gel state when maintained at 37 °C, as demonstrated by the test tube inversion method. Gelation was completed within the 36–37 °C range. The accelerated gel formation is attributed to early activation of hydrophobic interactions, which became increasingly dominant at higher temperatures, enhancing polymer chain collapse and network stabilization. In contrast, formulations with higher onset temperatures displayed slower gelation kinetics under identical thermal conditions. The sol–gel transition behavior of the selected formulation, CHI-PNIPAm-11, is illustrated in Fig. 2. This optimized system was selected for further experimentation and is referred to henceforth as CHI-PNIPAm.

3.5 Preparation of nanocomposite hydrogels

The CHI-PNIPAm-HZnO nanocomposite hydrogel was prepared by incorporating 0.5 wt% HZnO nanoparticles into the optimized formulation (formulation 11), which was based on a CHI : NIPAm : glutaraldehyde ratio of 20 mg : 200 mg : 8 μL. The suspension was maintained below 20 °C to prevent premature gelation and homogenized by stirring for 2 hours. Subsequent heating induced gelation, allowing assessment of changes in LCST, gelation time, and thermoresponsive behavior post-nanoparticle incorporation. Visually, the addition of HZnO increased the system's viscosity below the LCST, likely due to non-covalent interactions between the nanoparticles and the polymer matrix. Despite this, the LCST remained largely unchanged, possibly due to the relatively low nanoparticle concentration. The HZnO nanoparticles appeared to function as reinforcing agents, promoting a more structured and viscous network without significantly altering the thermal responsiveness of the hydrogel. The optimized HZnO content (0.5 wt%) was chosen to strengthen the network *via* hydrogen bonding and electrostatic interactions with chitosan functional groups while remaining below cytotoxic thresholds reported near 1 wt%. This nanoscale reinforcement improved mechanical stability and viscosity without significantly affecting the LCST.

The chosen HZnO content (0.5 wt%) balances mechanical reinforcement and biosafety: literature reports cytotoxic responses for ZnO NPs at concentrations in the low tens-to-hundreds of μg mL^{-1} (*i.e.*, orders of magnitude below 1% w/v), with Zn^{2+} release and ROS implicated as principal toxicity mechanisms. For this reason, we limited nanoparticle loading to 0.5 wt%, which in our hands produced no acute cytotoxicity in preliminary cell assays.

3.6 Spreadability analysis

The Line Spread Test (LST) was employed to evaluate the temperature-responsive flow behavior and viscosity changes of both the blank CHI-PNIPAm and the nanocomposite CHI-PNIPAm-HZnO hydrogels, demonstrating their potential for use in complex wound environments. At 20 °C, both hydrogels exhibited a low-viscosity, free-flowing liquid state, allowing for effortless dispersion. Upon exposure to 37 °C, the materials displayed a distinct sol–gel transition: the hydrogel initially flowed outward upon release but rapidly transformed into a stable, semi-solid state as viscosity increased. Quantitative line spread measurements, presented in Table 5, confirm a temperature-induced reduction in spread distance, indicative of increased viscosity and gelation. This thermal responsiveness ensures that, while the hydrogel remains fluid enough to fill and conform to irregular wound geometries upon application, it subsequently solidifies at body temperature to remain localized

Table 5 Line spread distance values of CHI-PNIPAm and CHI-PNIPAm-HZnO at 20 °C and 37 °C. Values represent mean ± S.D

Formulation	Temperature (°C)	Line-spread distance (cm)
CHI-PNIPAm	20	1.9 ± 0.058
	37	1.2 ± 0.1
CHI-PNIPAm-HZnO	20	1.67 ± 0.058
	37	1.0 ± 0.1

at the target site. Such dual behavior—initial spreadability followed by *in situ* gelation enables uniform coverage and retention within difficult-to-treat wounds. This balance between adaptability and structural stability is crucial for maintaining therapeutic contact and enhancing treatment efficacy in wound management applications.

3.7 Sol–gel fraction

The gel fraction values for CHI-PNIPAm and its nanocomposite counterpart, CHI-PNIPAm-HZnO, were determined to be 84.2 ± 0.1% and 85.0 ± 0.2%, respectively. The slight enhancement in gel content observed in the nanocomposite system suggests that the incorporation of HZnO nanoparticles may contribute to improved network formation. This effect is likely due to physical interactions between the nanoparticles and the polymer chains, which could facilitate more effective crosslinking and structural stabilization within the gel matrix.

3.8 Hydrogel swelling behavior and water retention capacity

Swelling behavior of both the unmodified (CHI-PNIPAm) and nanoparticle-loaded (CHI-PNIPAm-HZnO) hydrogels was assessed in phosphate-buffered saline (PBS) at pH 4 and pH 7.4, as shown in Fig. 3. Swelling ratios for all samples ranged between 200% and 330%, with greater expansion observed under acidic conditions (pH 4). This enhanced swelling is likely driven by increased protonation of chitosan's amine groups, which enhances hydrophilicity and promotes water uptake. In contrast, the nanocomposite hydrogel displayed a comparatively lower swelling capacity, attributed to a more compact and crosslinked polymeric network resulting from nanoparticle incorporation. Despite this, the nanocomposite retained moisture more effectively, possibly due to additional hydrophilic interactions introduced by the honey-derived ZnO nanoparticles within the matrix.

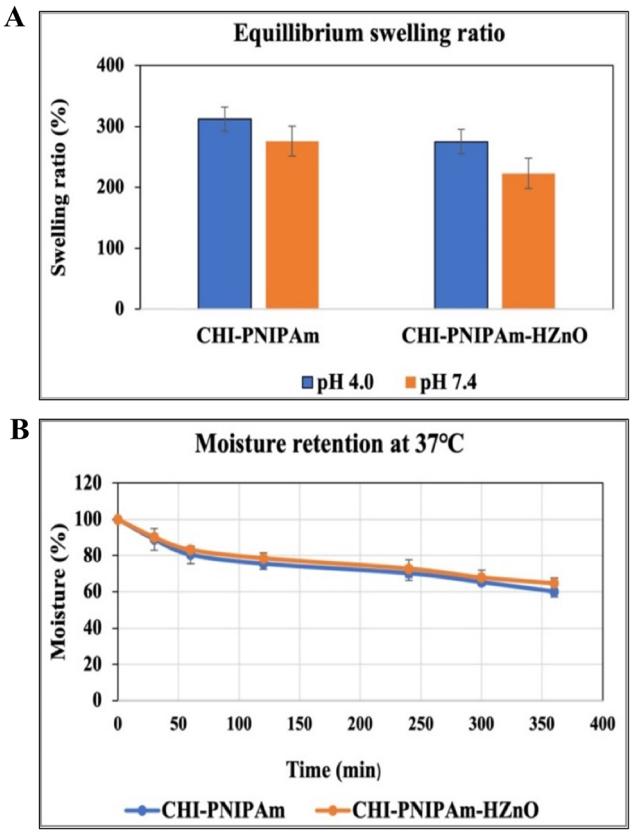

Fig. 3 (A) Equilibrium swelling ratio and (B) moisture retention at 37 °C of CHI-PNIPAm and CHI-PNIPAm-HZnO.

3.9 Scanning electron microscopy-based microstructural characterization of hydrogels

Scanning electron microscopy (SEM) revealed clear morphological differences between the CHI-PNIPAm hydrogel and its HZnO-loaded nanocomposite counterpart, as shown in Fig. 4. The unmodified CHI-PNIPAm hydrogel displayed a porous, crosslinked network typical of thermoresponsive hydrogels. However, several regions exhibited partially collapsed or compressed pores, likely resulting from polymer layer shifting or deformation during the drying and sample preparation processes. These distortions suggest that the blank hydrogel's network may lack sufficient mechanical resilience to withstand preparation-related stresses, leading to structural collapse during sectioning or mounting. In contrast, the CHI-PNIPAm-HZnO nanocomposite exhibited a more textured and granular surface morphology with an inset of clustered nanoparticles as shown in figure. Spherical HZnO nanoparticles were visible both on the surface and embedded within the hydrogel matrix, appearing as fine particulate matter or as distinct aggregates and bright clusters. The overall porous architecture of the nanocomposite appeared more intact and uniformly distributed, indicating improved network stability. Further, the CHI-PNIPAm-HZnO with DPMSCs showed embedded cells in the hydrogel. This enhanced definition and surface roughness suggest a higher crosslinking density, likely reinforced by the presence of ZnO, contributing to the nanocomposite's superior structural integrity relative to the blank hydrogel.

3.10 X-ray diffraction based crystalline phase identification in hydrogel systems

The X-ray diffraction (XRD) profile of individual components CHI, NIPAm, and HZnO as well as their respective polymeric and nanocomposite formulations are represented by Fig. 5. The diffraction pattern of chitosan (CHI) is marked by a broad hump centered near $2\theta \approx 20°$, which is characteristic of its semi-crystalline structure, where amorphous regions dominate due to the irregular packing of polymer chains. In contrast, NIPAm displays sharp, well-defined peaks in its XRD pattern, indicative of its highly crystalline monomeric nature. HZnO exhibits a series of intense and distinct peaks at 2θ values of approximately 31.8°, 34.4°, and 36.2°, corresponding to the (100), (002), and (101) planes, respectively—hallmarks of the hexagonal wurtzite crystal phase of ZnO. Upon formation of the CHI-PNIPAm hydrogel, the resulting diffraction pattern reflects a hybrid structure: the broad amorphous peak from chitosan is retained, while multiple sharp peaks attributed to PNIPAm crystallinity remain clearly visible. This indicates that the polymerization of NIPAm onto the chitosan

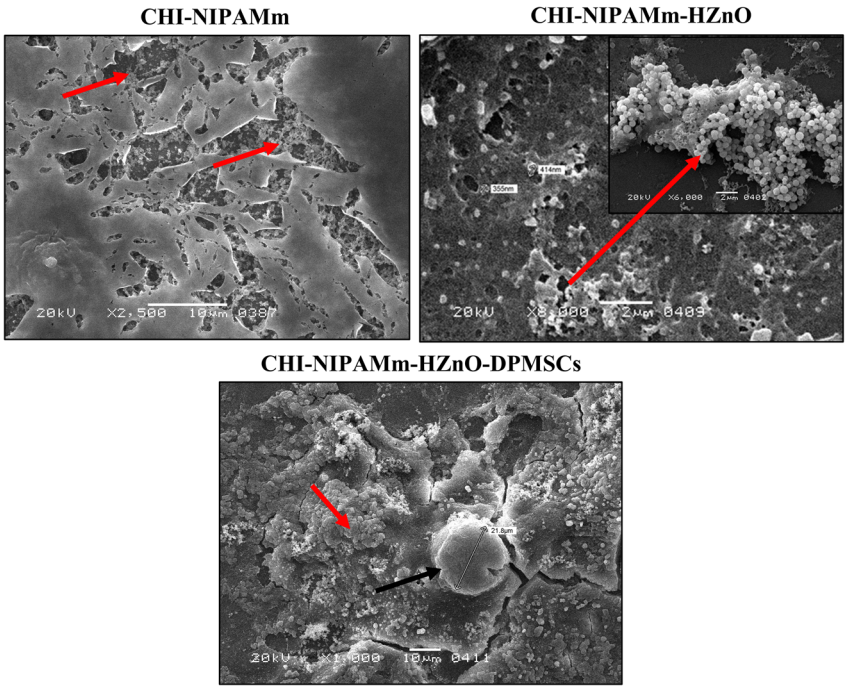

Fig. 4 Scanning electron micrographs. The images showed the hydrogel surface morphology marked with red arrow heads in all the groups without HZnO nanoparticles and DPMSCSs. The CHI-PNIPAm-HZnO showed distribution of HZnO nanoparticles with and inset at higher magnification showing clustered hydrogel with HZnO. The PNIPAm-HZnO/DPMSCs showed incorporation of cells in hydrogel marked with red arrow heads and measurement of cell size as 21.8 μm.

backbone does not fully suppress its ordered domains. Instead, PNIPAm chains are likely present in a semi-crystalline state within the amorphous chitosan matrix, suggesting partial preservation of crystallinity following copolymer formation. Interestingly, in the CHI-PNIPAm-HZnO nanocomposite, while the overall pattern still reflects both the amorphous halo of chitosan and the residual crystallinity of PNIPAm, the characteristic peaks of ZnO observed in the pristine HZnO sample are notably absent. This loss of crystalline signal from ZnO could be due to its nanoscale dispersion within the polymer network or structural changes upon incorporation. Similar effects have been reported in other nanocomposite systems, where strong interactions with polymer chains or surface functionalization lead to peak broadening, amorphization, or reduced crystallite size below the XRD detection threshold.[41]

3.11 Thermogravimetric analysis-based thermal stability assessment of hydrogels

Thermogravimetric analysis (TGA) was conducted to assess the thermal stability of individual components CHI, NIPAm, and HZnO as well as the synthesized CHI-PNIPAm and CHI-PNIPAm-HZnO hydrogels, with the resulting thermograms displayed in Fig. 6. Each material was analyzed over a temperature range from ambient conditions to 600 °C. Chitosan exhibited a characteristic two-step degradation pattern. The initial weight loss observed below 100 °C corresponds to the release of bound moisture, a common feature of hydrophilic polysaccharides. A significant mass loss occurs between 250 °C and 400 °C, attributed to the thermal breakdown of its glycosidic linkages and polymer backbone. Beyond this, CHI continues to degrade at a slower rate, leaving approximately 32% of its mass as residue at 600 °C, reflecting its relatively high thermal resilience. In contrast, *N*-isopropylacrylamide (NIPAm) showed a sharp and rapid decomposition event, with the bulk of its mass lost below 200 °C. This steep decline reflects the thermolability of the monomeric form, which undergoes complete volatilization with negligible residual content, consistent with its low molecular weight and simple structure. The thermal profile of honey-synthesized ZnO (HZnO) revealed a more gradual, continuous weight loss across the full temperature range. This slow degradation trend is comparable to that observed in other reports of biosynthesized ZnO nanoparticles, where organic residues from biological precursors, such as honey, contribute to persistent weight changes.[40] The continuous decrease in weight loss may be due to the decomposition of thermo-labile organic capping agents (*e.g.*, sugars, proteins, or polyphenols), which is an inherent feature of the bio-reduced nanoparticles, compared to their chemically reduced counterparts.[35] The thermogravimetric profile of the copolymer CHI-PNIPAm exhibits a multi-phase degradation, corresponding to the thermal degradation of chitosan and PNIPAm separately, and an initial weight loss below 100 °C related to water removal. This is followed by a broad degradation phase spanning 200–400 °C, corresponding to the breakdown of the copolymeric network. Unlike pure chitosan, which degrades within a narrower range, the extended degradation window in the copolymer suggests intermolecular interactions between the PNIPAm chains and the chitosan backbone that slightly enhance its thermal durability. Beyond 400 °C, a sharper mass reduction is

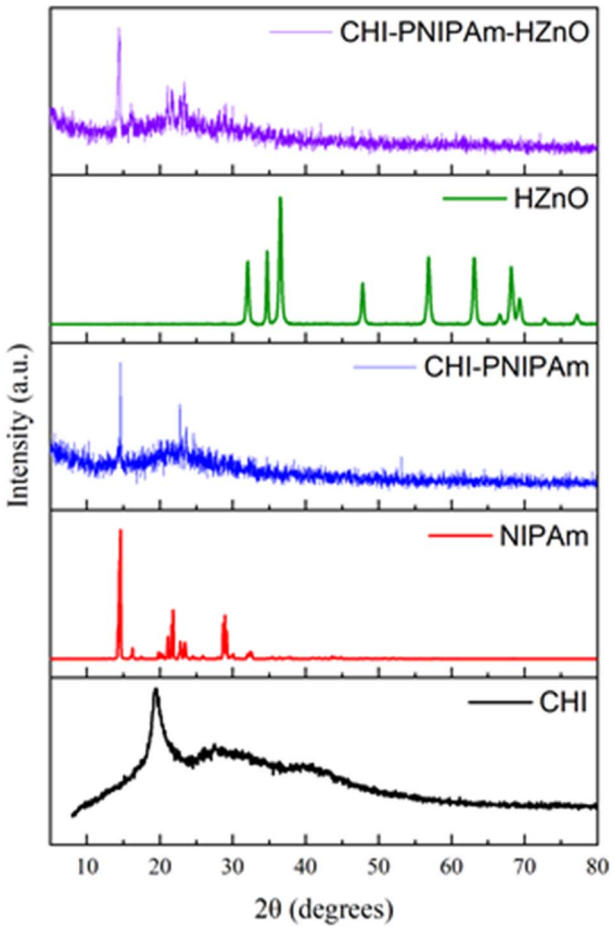

Fig. 5 X-ray diffractograms of CHI, NIPAm, HZnO, CHI-PNIPAm and CHI-PNIPAm-HZnO.

observed, leaving around 7% residue at 600 °C, indicating improved thermal resistance compared to NIPAm alone, largely due to the structural contribution of chitosan. The CHI-PNIPAm-HZnO nanocomposite exhibits a similar thermal decomposition profile, with subtle but notable differences. As in the copolymer, the first phase of moisture loss occurs below 100 °C. Major decomposition takes place between 200 °C and 400 °C, associated with the degradation of organic polymer chains. A steeper weight loss is noted between 400 °C and 450 °C, but the nanocomposite retains about 18% of its original mass at 600 °C more than double that of the blank hydrogel. This enhanced thermal stability is likely due to the incorporation of honey-derived ZnO nanoparticles. These particles not only impede heat flow through the matrix, acting as insulative barriers, but may also facilitate additional non-covalent cross-linking within the hydrogel, restricting polymer mobility and slowing thermal degradation. Overall, the incorporation of HZnO improves the thermal robustness of the hydrogel system, ensuring sufficient stability for biomedical applications where exposure to elevated temperatures during storage or sterilization may occur.

3.12 Chemical bonding and functional group analysis using FTIR spectroscopy

Fourier-transform infrared (FTIR) spectroscopy was employed to investigate the chemical interactions and functional groups present within the CHI-PNIPAm-HZnO hydrogel system, with the resulting spectra shown in Fig. 7. In the spectrum of pure chitosan, a broad absorption band centered around 3279 cm^{-1} corresponds to O–H stretching vibrations, indicative of intermolecular hydrogen bonding. The peak observed at 1579.7 cm^{-1} is attributed to N–H bending, while the signal at approximately 1020 cm^{-1} is associated with C–O stretching vibrations, typical of polysaccharide backbones. The FTIR spectrum of honey-derived ZnO nanoparticles (HZnO) reveals multiple functional groups derived from organic constituents present in honey. A prominent band near 3000 cm^{-1} indicates O–H stretching from hydroxyl-containing compounds such as alcohols, phenols, and organic acids. A moderate peak around 1700 cm^{-1} is ascribed to carbonyl (C=O) stretching, likely due

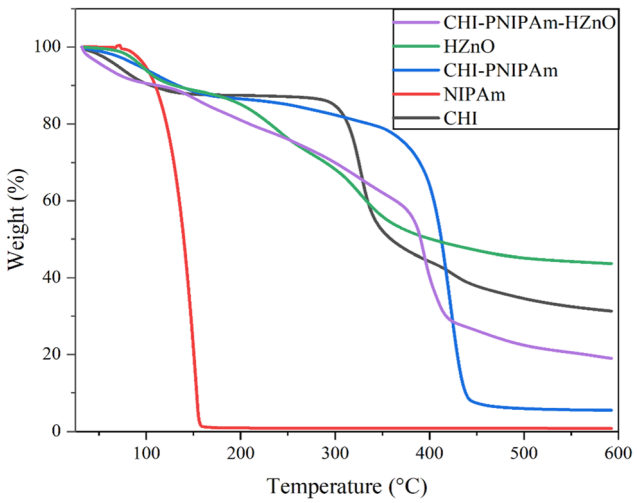

Fig. 6 TGA curves of CHI, NIPAm, HZnO, CHI-PNIPAm, CHI-PNIPAm-HZnO.

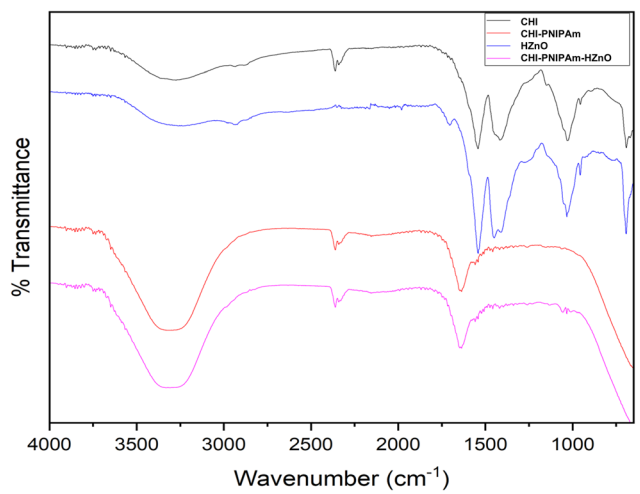

Fig. 7 FTIR spectra of CHI, HZnO, CHI-PNIPAm and CHI-PNIPAm-HZnO.

to gluconic acid or related compounds. The absorption near 1600 cm^{-1} may reflect N–H bending of amine groups or asymmetric stretching of carboxylates. Peaks in the 1400 cm^{-1} region correspond to C–O–H bending modes from protein residues. Additionally, vibrations in the 1200–1150 cm^{-1} range are attributed to C–N stretching (amide groups) and C–O stretching in proteins, while signals between 1000–1100 cm^{-1} are characteristic of C–O stretching from alcohols, esters, and carbohydrates.[42] A distinct absorption band emerging at 1650 cm^{-1} in the FTIR spectra of both CHI-PNIPAm and CHI-PNIPAm-HZnO hydrogels signifies the presence of imine (C=N) functional groups. The absorption band observed around 1650 cm^{-1} can be attributed to overlapping contributions from the amide I (C=O) stretching vibration of PNIPAm and the C=N stretching vibration of imine linkages formed *via* Schiff base condensation between chitosan amino groups and glutaraldehyde aldehyde groups. Thus, relative to chitosan, the FTIR spectra provide diagnostic evidence of chemical modification and hydrogel formation. The typical C–O–C and C–O stretching bands of chitosan observed around 1000–1100 cm^{-1} were not evident in chitosan-g-PNIPAm, likely due to overlapping with strong amide vibrations of PNIPAm and partial substitution of hydroxyl groups during grafting. However, a slight indentation reappears in this region for the chitosan-g-PNIPAAm/HZnO composite, which can be attributed to ZnO-induced interactions or coordination with residual hydroxyl functionalities of chitosan.

3.13 Force-dependent injectability testing of hydrogel systems

The injectability of both CHI-PNIPAm and CHI-PNIPAm-HZnO formulations was evaluated by extruding them through 22G and 23G needles at controlled flow rates of 1 and 2 mL min^{-1}. As expected, a direct correlation was observed between the applied flow rate and the required injection force— higher flow rates demanded greater force. In addition, needle gauge significantly influenced injectability: the 22G needle consistently required lower force than the narrower 23G needle across all conditions tested. This difference is attributed to the wider internal diameter of the 22G needle, which facilitates easier passage of the hydrogel, particularly in formulations with higher viscosity. In contrast, the smaller bore of the 23G needle imposed greater resistance, resulting in higher force requirements to achieve the same delivery rate. These findings highlight the influence of delivery parameters on formulation performance and support the feasibility of syringe-based administration for both hydrogel types.

3.14 Isolation and characterization of human dental pulp derived mesenchymal stem cells (DPMSCs)

3.14.1 Isolation and culturing of DPMSCs. The isolated cells were obtained from the explant culture after 15 days, and the isolated cells showed a high proliferation rate and 70–80% confluency in a T-25 culture flask within a week at passage 0 as shown in Fig. 8A and B. Later, the cells were sub-cultured in a T-75 culture flask depending on the cell density and achieved 80% confluency within 4 to 5 days at passages 1 and 2 (Fig. 8C–F). The observed cells showed fibroblast-like morphology.

3.14.2 Immunophenotyping. The cells were then characterized at passage 3 using immunocytochemistry. DPMSCs showed positive results for CD44, CD90 and CD105 confirming presence of mesenchymal stem cell surface markers, whereas CD45 showed negative results which is a hematopoietic stem cell surface marker. The results obtained confirms the isolation of single, homogeneous population of DPMSCs as shown in Fig. 8G.

3.14.3 Trilineage differentiation characterization. The cells grown in a specialized medium during trilineage differentiation showed unique markers indicating their development into three separate cell types. Mineral deposits after alizarin red staining verified the differentiation into osteocytes, responsible for mineralization and bone production. Comparably, ol red O labelling produced noticeable oil droplets, confirming their differentiation into adipocytes. Ultimately, proteoglycans were detected by alcian blue staining, which demonstrated their effective differentiation into chondrocytes as shown in (Fig. 8H).

The methods used to analyze dental pulp stem cells correspond with other published results on their application for regenerative therapies. Our laboratory tests showed the isolated cells were of mesenchymal lineage since they expressed CD44, CD90, CD105 markers but not CD45. These tests show the typical features of MSCs and confirm the ability to create a homologous DPMSCSs group.[43] Using specific stains, the research demonstrated that DPMSCSs can transform into osteocytes adipocytes and chondrocytes.[44]

3.15 Cytotoxicity of hydrogel on DPMSCs

Analysis of cell viability and cytotoxicity of DPMSCs treated with different concentrations of thermoresponsive blank hydrogel (CHI-PNIPAm) and honey hydrogel (CHI-PNIPAm-HZnO) was performed after 24 hours of MTT assay. The assay showed the decrease in cell survival percentage with the increase in hydrogel concentration. It was observed that at concentration of 700 μg mL^{-1} maximum cell survival rate of 20% was observed in CHI-PNIPAm which was reduced down to 4% at 5000 μg mL^{-1} compared to control (Fig. 9A). However, in contrast to CHI-PNIPAm a significant increase was observed in cell survival rate of CHI-PNIPAm-HZnO with increasing concentration *i.e.* 60% cell survival rate at 1000 μg mL^{-1} which increased up to 128% at maximum concentration of 5000 μg mL^{-1} compared to control (Fig. 9B).

The cell viability test showed the mesenchymal stem cells suffered decreasing survival rates as hydrogel exposure increased. The honey hydrogel (HH: CHI-PNIPAm-HZnO) showed a surprising result by making MSCs thrive better at increasing concentrations up to 128% at 5000 μg mL^{-1}. It showed unique benefits for MSC survival since it helps the cells thrive. Previous research shows that adding more hydrogel to cell cultures creates harmful conditions that affect cell growth rates which is in accordance with our results of blank hydrogel.[45] Although chitosan-based hydrogels show high

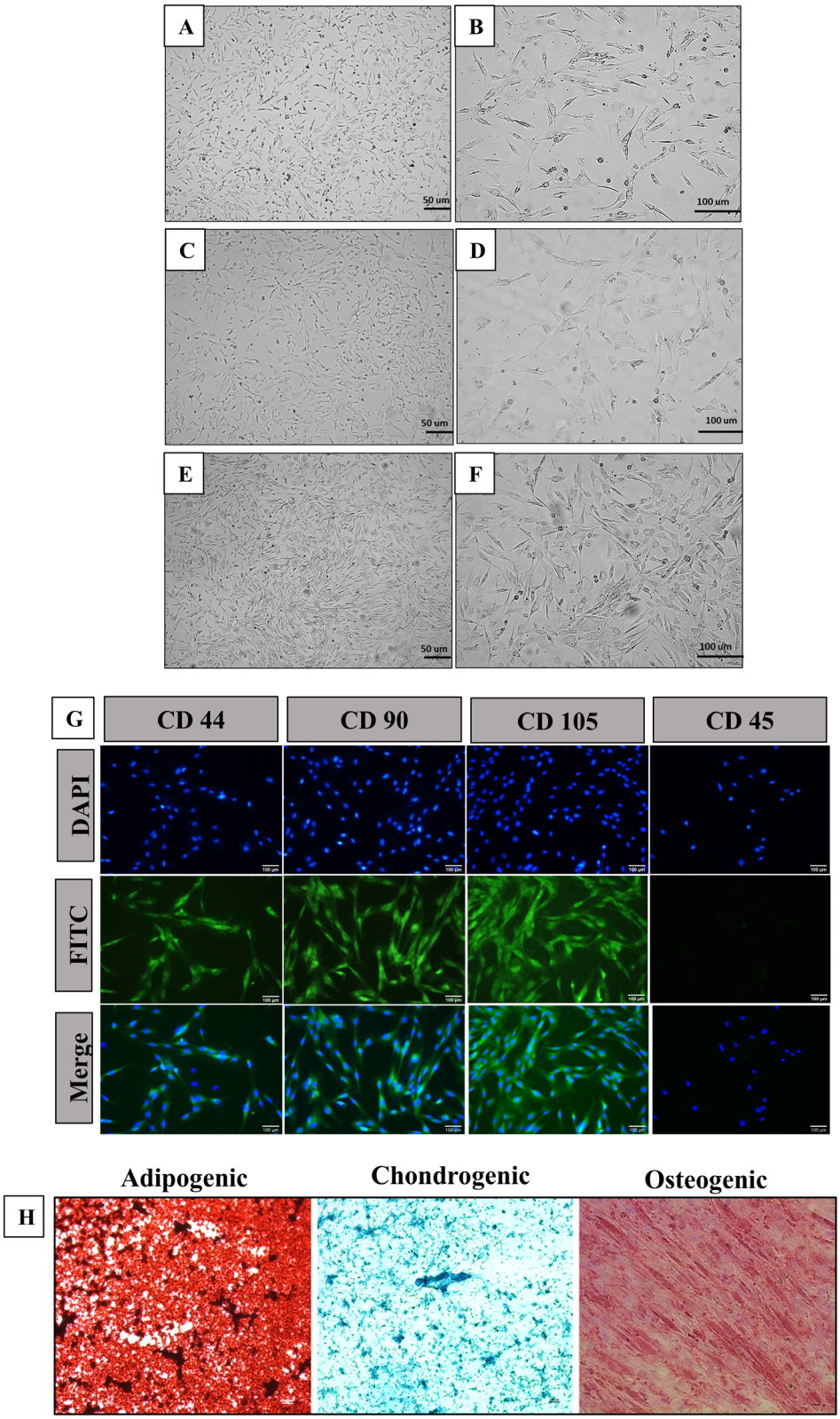

Fig. 8 Morphology and characterization of DPMSCs. DPMSCs showed fibroblast like morphology at P0 on 7th day of culture (A and B). The cells at P1 showed fibroblast like morphology with small extensions (C and D) and obtained 70–80% confluency when subcultured for next passage 2 (E and F). The images were taken at 4× and 10× magnification. Fluorescent images of isolated DPMSCs characterized by immunocytochemistry using specific markers CD44, CD90, CD105, and CD45 (negative marker) are shown with DAPI stained nuclei and merged images (G). DPMSCs stained with oil red O showing oil droplets (adipogenic), alician blue showing proteoglycans (chondrogenic) and alizarin red stain showing mineral deposits (osteogenic) differentiation of DPMSCs cultivated in specialized media (H). The images were taken at 10× magnification.

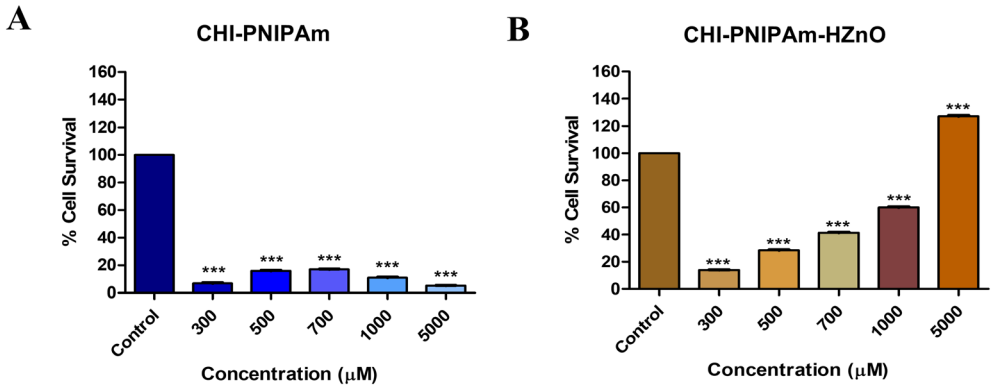

Fig. 9 Cytotoxicity analysis by MTT assay. The graph shows concentration dependent effect on the viability of DPMSCs. Significant decrease in the viability was observed at higher concentration (A) and significant increase in the cell viability was observed at higher concentration compared to control (B). One way ANOVA was used for statistical analysis, followed by Bonferroni's *post hoc* test and *P* value of < 0.05 was considered statistically significant compared to control (where *** = $p < 0.001$).

biocompatibility like other biomaterials they have dose-related negative impact on cells that happens when many polymers crowd together and block oxygen-nutrient transport to cells.[46] Honey benefits as a natural anti-inflammatory compound, and also allows cells to multiply readily. Research shows honey-based pharmaceuticals boost tissue regeneration through enhanced blood vessel development while fighting cell damage, and multiplying essential cells.[47,48] The higher level of 5000 μg mL^{-1} bioactive compounds from honey including flavonoids and phenolic acids enhance cell survival because they also mitigate the damaging effects of excess polymer concentration.

3.16 Macroscopic visualization of control and treated burns

3.16.1 Control burn. The control burn was observed for 2 weeks from both dorsal and ventral side. At day 1 of burn infliction mild edema was observed which increased till day 3

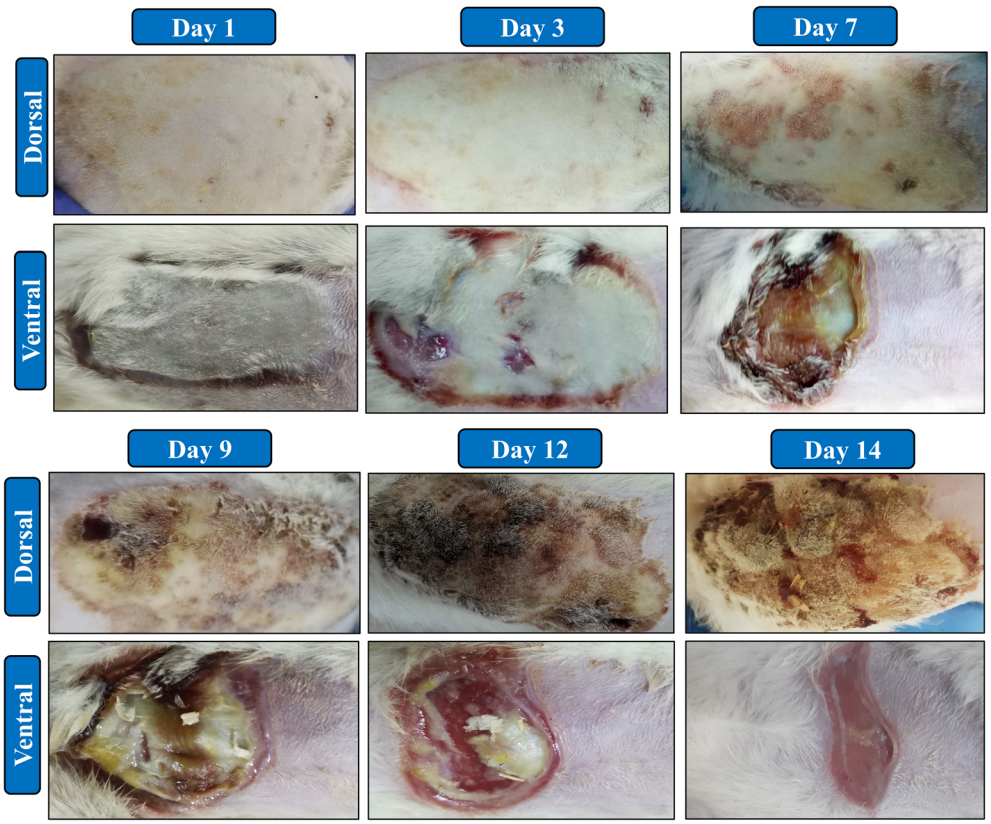

Fig. 10 Macroscopic visualization of control burn. severe edema was observed at day 1 extending to day 3. At day 6 and 9, the wound progressed with coagulation and hyperemia. Further at day 12 and 14, a thick scab formation was observed at dorsal surface with scab detachment at ventral surface.

following the zone of stasis. From day 6 to 12 onwards zone of coagulation was observed which was increasing in a time dependent manner leading to a formation of thick scab on the dorsal surface, which was not detached until day 14. However, on the ventral surface the zone of coagulation was observed till day 9 following the formation of mild scab, detached till day 12 leading to partial wound healing till day 14 (Fig. 10).

Observations of the control burn healing over 21 days in rats concur with an expected course of burn healing as the wounds undergo formation and maturation of epidermis and granulation tissue, along with contraction. The edema continues to rise until day 3, this is due to the initial inflammatory response of the body to the injury, which is followed by the formation of a zone of coagulation, leading to tissue necrosis that progresses and develops into a thick eschar (scab). However, interestingly, there is difference in progress of healing between the dorsal and ventral surfaces. Thicker skin on the dorsal surface may also increase the zone of coagulation and may decrease the rate of healing.[49] Also, improved vascularity of the ventral side might favor rapid healing.[50] The more persistent eschar on the dorsal side until day 14 indicates that the burn was deeper or more severe compared to the burn on the ventral side. This could partly be because the dorsal area has a less substantial blood supply than the ventral surface and corresponds to the region where rapid detachment was observed.

3.16.2 DPMSCs treated burn wound. At day 3 post DPMSCs transplantation the burn healing progression was observed at both dorsal and ventral surface. Mild zone of coagulation was observed till day 7 compared to control, and the thick scab formed started to detach till day 14 on the dorsal side. However, on the ventral side, scab detachment was observed till day 7 and till day 14 about 80% wound closure was observed compared to control (Fig. 11). Consequently, these results show the predictive values of DPSMCs and thermoresponsive hydrogels for improving burn wound healing. This accelerated healing of the DPMSCSs treated group, with earlier scab detachment and wound closure compared to the control is evidence of DPMSCSs' enhanced tissue regeneration capabilities.

3.16.3 Thermoresponsive hydrogel treated burn wound. The blank hydrogel; (CHI-PNIPAm) transplanted burn wound, described previously in Section 2.2.17 showed significant zone of hyperemia and mild zone of stasis following zones of coagulation in the overall region of the wound at day 7 post transplantation. At day 14, the zone of coagulation was elevated throughout the wound (Fig. 11). In contrast to this, the ventral side showed signs of healing till day 14, with elevated zone of coagulation (Fig. 11). The honey hydrogel; (CHI-PNIPAm-HZnO) transplanted wound showed increased edema with elevated zone of stasis at post transplantation (day 1) followed by zone of coagulation at day 7 (Fig. 11), whereas, at day 14, mild scab detachment was observed indicating the burn healing progression compared to the blank hydrogel on the dorsal side (Fig. 11). Increased edema with mild zone of coagulation was observed initially, increased till day 7 and mild scab detachment was observed from wound surroundings whereas, till day 14, partial wound closure was observed on the ventral surface (Fig. 11).

3.16.4 Thermoresponsive hydrogel with DPMSCs treated burn wound. The CHI-PNIPAm with DPMSCs transplanted burn wounds as described previously in Section 2.2.17 showed significant zone of hyperemia and zone of stasis post transplantation (day 1) following mild zone of coagulation till day 7 (Fig. 11). At day 14, the zone of coagulation was elevated throughout the wound with thick scab formation and mild detachment with hair growth which indicated healing progression on the dorsal side (Fig. 11). In contrast to this, the ventral side showed elevated zone of coagulation till day 7 followed by mild scab detachment at day 14 (Fig. 11). The treatment CHI-PNIPAm-HZnO/DPMSCs transplanted wound on the dorsal surface showed elevated zone of stasis post transplantation followed by zone of coagulation and scab formation till day 7 (Fig. 11). At day 14, mild scab detachment was observed indicating the healing progression (Fig. 11). On the ventral surface, increased edema was observed initially followed by elevated zone of coagulation with mild scab detachment till day 7, whereas, re-epithelialization with partial wound closure was observed till day 14 (Fig. 11).

The effects of the different types of thermoresponsive hydrogels are different.[9] The blank hydrogel (CHI-PNIPAm) did not show an improved wound healing over the control group, but the honey incorporated hydrogels showed significantly much better healing, especially on the ventral side of the wound. The improved healing could be explained by the anti-inflammatory effect of the honey hydrogel (CHI-PNIPAm-HZnO), as discussed.[51] Additionally, the combined use of the thermoresponsive hydrogels with DPMSCSs improved healing outcomes, in particular in the presence of honey. This indicates that there might be additive or synergistic effect between the stem cells and the hydrogel delivery system, however some confounding factors might exist. As reported that application of topical honey and systemic zinc in combination increases re-epithelialization, vascularization and collagen deposition in full thickness excision wound.[52] Similarly, in terms of dressings based on honey and loaded with ZnO nanoparticles also demonstrates increased antibacterial activity and mechanical stability profile compared to honey alone.[53] In terms of stem cells, honey or ZnO also effects the migration and proliferation of cells positively or negatively by interacting with the signaling pathways and changing the cellular behavior, however further mechanistic studies needed to confirm the mechanism of synergy. Therefore, since our data is consistent in demonstrating the enhances therapeutic effect of the combined treatment which is reflected more as an additive effect and synergistic in only certain conditions. And these combinations did show enhanced healing where there was hair growth, scabs coming off and re-epithelialization, which speaks to potentially better functional and aesthetic wound healing outcomes in burns. Because the blank hydrogel + DPMSCSs combination did not show significant improvement, the composition of the hydrogel seems to be important for promoting healing.

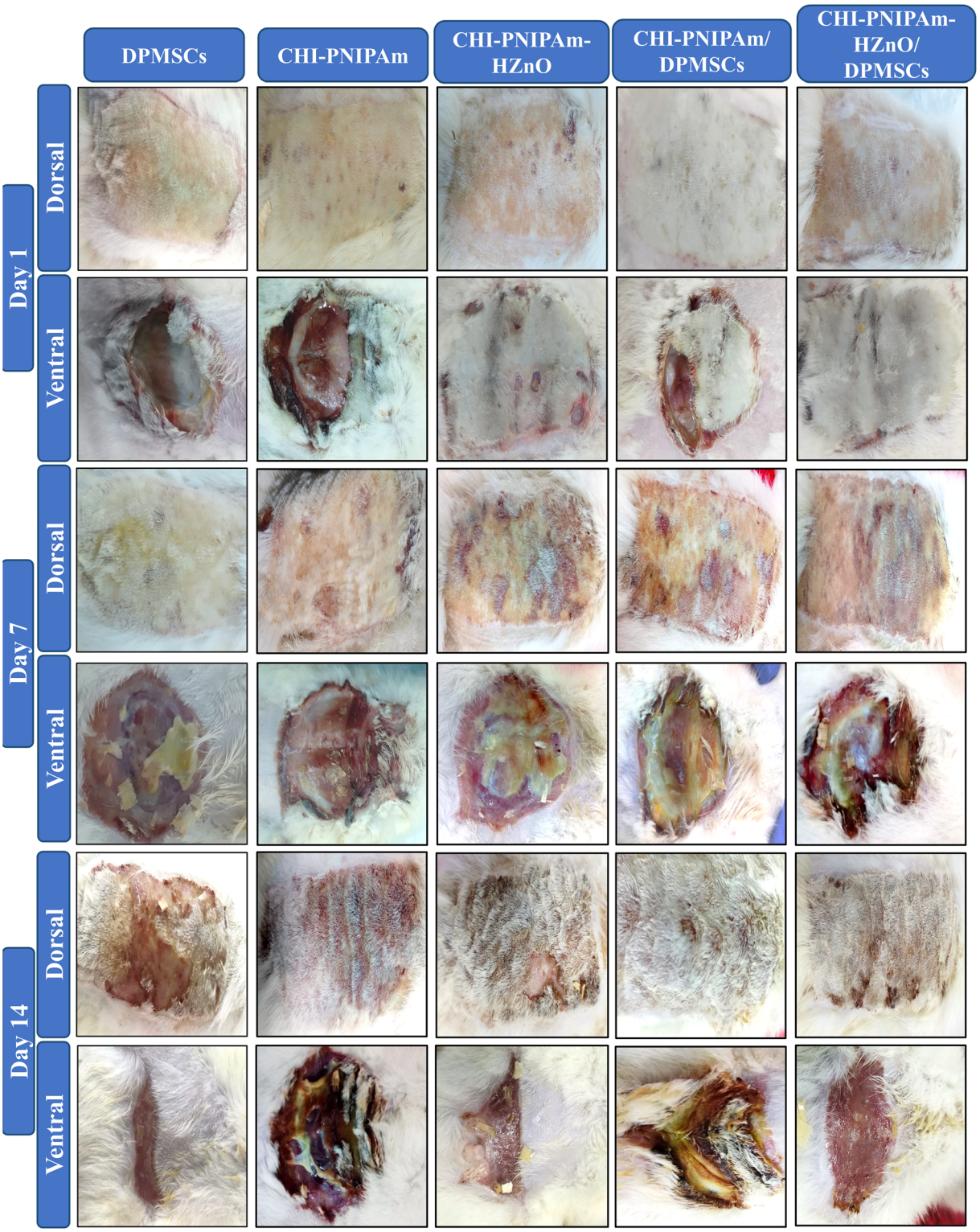

Fig. 11 Macroscopic visualization of treated burn wounds. At day 1 of DPMSCs transplantation, edema was disappeared and few zones of coagulation was observed till day 7. Further, at day 14, scab detachment was observed at dorsal side, whereas wound healing was observed at the ventral side. The CHI-PNIPAm treated wound showed mild edema with moderate zone of coagulation as the burn healing progresses from day 1 to day 7. In CHI-PNIPAm-HZnO, wound showed a moderate zone of stasis at day 1 which leads to moderate coagulation till day 7 at the dorsal side, whereas, thick scab formation was observed till day 14. The CHI-PNIPAm/DPMSCs treated wound showed severe edema on day 1, progressing to severe stasis and coagulation till day 7, and scab formation at day 14. The wound showed moderate hyperemia which led to moderate coagulation till day 7 and minor scab detachment on day 14.

3.17 Histopathological analysis

3.17.1 Control burn. The control burn histopathological analysis was performed on day 1, 3, 7, 12, 14 and 21 (SI Fig. S2). Initially, at post burn infliction, mild inflammation and collagen disruption was observed in the epidermis, followed by increased inflammation and collagen destruction till day 3, whereas, from day 7 to 12 disrupted collagen with highly inflamed hair follicles was observed. Further, at day 14, deep scar formation was observed originating from epidermis and expanding till dermis (Fig. 12B). However, the burn scarring disappeared till day 21 and wound healing progression was observed, showing signs of re-epithelialization and collagen deposition as shown in SI Fig. S2. Similarly, the ventral side in control burn showed nearly similar results. At day 1 and 3 moderate inflammation with severe collagen impairment was observed (SI Fig. S2). At day 7 the tissue architecture was completely degraded with highly inflamed hair follicles (Fig. 12B). Further at day 12 and 14 the tissue framework shows signs of degradation as a result of chronic inflammation and at day 21, re-epithelialization was observed with increased inflammation in epidermis and hair follicles (SI Fig. S1). The control burn showed the pathophysiology of the burn wounds healing through the period of 21 days by histopathological analysis. The observations from both dorsal and ventral sides in the control burn reveal key phases of inflammation, collagen disruption and regeneration, re-epithelialization, and scar formation.

Days 1 and 3 show normal early inflammatory reactions and loss of collagen as thermal wounds stimulate these factors.[54] On day 3, the damage becomes severe as a part of natural healing process initiated by inflammation. Hair follicles become inflamed on day 7 as research shows they participate remarkably in wound recovery by promoting natural healing mechanism using growth factors stored in follicles.[55] The inflammation developed surrounding hair follicles demonstrates their direct participation in wound repair activities.[56] Standard burn assessment reveals that deep scars emerge on day 14 from the surface layer to penetrate the bottom layer in large wound injuries.

The wound healing process finished successfully when scars faded on day 21 and new skin formed along with new collagen at this stage which aligns with the normal burn recovery. Our results show that although the ventral side matches the dorsal side in early inflammation and collagen damage, the delayed healing and ongoing inflammation indicate slower recovery.

3.17.2 DPMSCs treated burn wound. The burn wounds treated with DPMSCs were examined over a 2 weeks period at days 7 and 14 post-treatment, assessing both the dorsal and ventral sides of the wounds. On the dorsal side of the wound the inflammation was reduced in both the epidermis and hair follicles as well as collagen deposition was observed compared to the control burn at day 7. Mild scarring was observed originating from the epidermis and extending till dermis with infiltration of inflammatory cells; however, the collagen matrix deposition regenerated the framework of the skin tissues leading to remodeling till day 14. In contrast, the ventral side of the treated wound exhibited moderate inflammation throughout the epidermis and dermis along with impaired collagen matrix in the 1st week. By day 14, inflammation had diminished, fibroblast migration was observed, and the process of tissue architecture restoration had begun compared to the control burn (Fig. 12C). Insights on improved healing were observed with the treatment of DPMSCs on burn wounds. The reduced inflammation coupled with observed collagen deposition seen on dorsal side at day 7, relative to the control suggests an accelerated healing process. It is well known that DPMSCs possess potent anti-inflammatory and immunomodulatory properties.[57] They facilitate to reduce the inflammation around the wound bed, thereby making a more favorable environment for tissue regeneration. Further, some scar formation is unavoidable, the DPMSCs might enhance a more organized and functional collagen matrix that could result in better scar conditions as observed till day 14.[58] The results of this study are consistent with studies addressing the effect of growth factors on burn wound healing.[59]

3.17.3 Thermoresponsive hydrogel treated burn wound. The honey (CHI-PNIPAm-HZnO), blank (CHI-PNIPAm) hydrogels treated burn wounds were examined from both dorsal and ventral side for a period of 2 weeks. The blank hydrogel showed reduced inflammation with disrupted collagen and scar formation, whereas, honey hydrogels showed reduced inflammation with decrease in infiltration of inflammatory cells and deposition of collagen on the dorsal side at day 7 (Fig. 12D and E). The second week post treatment with blank hydrogel showed deep scarring with increased infiltration of inflammatory cells (Fig. 12D). However, the honey hydrogel exhibited restoration of the skin tissue architecture with the increase in collagen matrix deposition and migration of fibroblasts both on dorsal and ventral sides till 2nd week post treatment (Fig. 12E). In contrast, the ventral side of the wound treated with blank hydrogel showed similar results as of dorsal side, exhibiting collagen impairment at first week and moderate inflammation followed by damaged tissue architecture and scarring (Fig. 12D). These observations indicate that the honey constituent may play a significant role in improving the rate of healing that may be associated with the antimicrobial and anti-inflammatory effects of honey.[60] Also, the blank hydrogel presented the least comparable healing to honey hydrogels.

3.17.4 Thermoresponsive hydrogel with DPMSCs treated burn wound. The blank hydrogel (CHI-PNIPAm/DPMSCs) showed infiltration of inflammatory cells in hair follicles and collagen disruption in the first-week post-treatment, which was further increased by the second week (Fig. 12F). The honey hydrogel (CHI-PNIPAm/HZnO/DPMSCs) showed a significant reduction in inflammation, collagen deposition, and epidermis formation at first week followed by tissue framework regeneration and complete re-epithelialization leading to the development of functional skin, second week (post treatment) on the dorsal side (Fig. 12G). In contrast, the ventral side of CHI-PNIPAm/DPMSCs showed increased inflammation on the first week of treatment whereas, reduced inflammation, restoration of the collagen matrix, and complete re-epithelialization were observed on second week (Fig. 12F). The results of honey hydrogel with DPMSCs, showed reduction in inflammation and increased fibroblast migration at week 1 and 2 respectively (Fig. 12G).

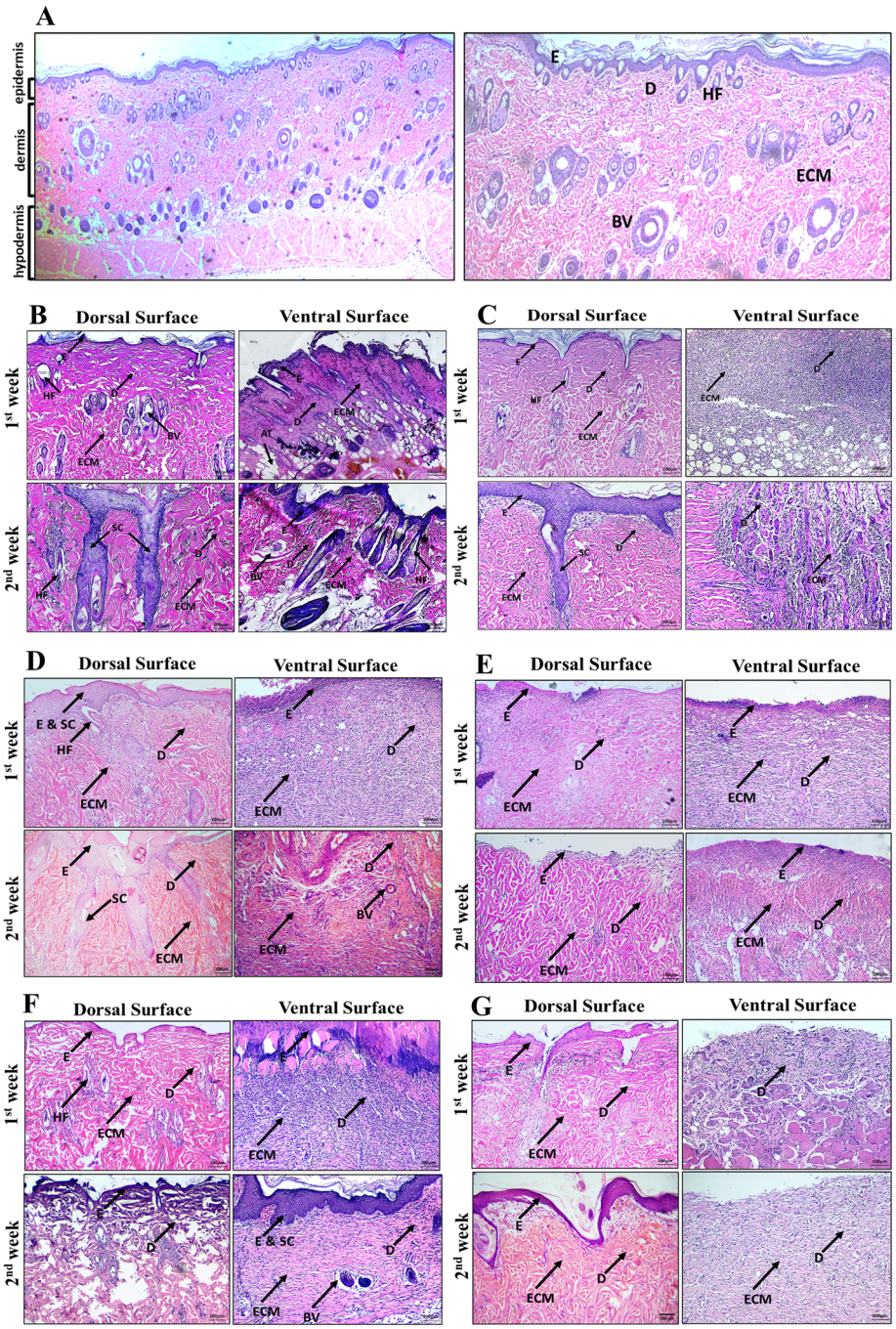

Fig. 12 Histological analysis of normal skin, control burn and treated groups. Normal skin morphology is shown at magnifications of 4× and 10× (A). The control burn showed inflamed and disoriented tissue framework which progressed with damaged ECM and inflamed hair follicles at 1st week, whereas, severe tissue scarring leading to incomplete regeneration was observed at 2nd week (B). The histology of DPMSCs treated burn showed complete regeneration of the skin tissue till 1st week, however till 2nd week, tissue scarring was observed at dorsal side. The ventral surface showed moderate inflammation leading to incomplete organization of the skin tissue till 2nd week (C). Mild inflammation with a disoriented tissue framework at week 1, whereas, severe scarring was observed at 2nd week at both dorsal and ventral surfaces (D). In the honey hydrogel group deposition of ECM with the migration of fibroblast cells was observed till day 14 in both dorsal and ventral surfaces (E). Severe inflammation was observed on the ventral and dorsal surface with disrupted tissue morphology on the 1st and 2nd week of treatment, respectively (F). In honey with DPMSCs treatment, ECM formation was observed after 1st week leading to remodeling of the tissue framework whereas, on the ventral side mild inflammation with ECM deposition was observed till 2nd week of treatment (G). The tissue structures are labeled as epidermis (E); dermis (D); hair follicles (HF) and extracellular matrix (ECM), blood vessels (BV) and scarring (SC). The images were taken at 10× magnification.

The combination of honey hydrogel with DPMSCs demonstrated visible enhancements in the wound healing on the dorsal side exhibiting complete re-epithelialization and functional skin architecture; however, with the employing of the blank hydrogel with DPMSCs, the outcome was not satisfactory. This means that DPMSCs and the components of the hydrogel should work in coherence to enhance the healing outcome. These results comply with other studies that report the potential of cells as a therapeutic agent in adopting biomaterials like honey hydrogel.[61]

3.18 Gene expression profiling

3.18.1 Control burn. The gene expression analysis of inflammatory cytokines involving the expression of IL-1β and IL-6 showed a significant increase in the expression levels compared to control. At days 1 and 3 post burn IL-1β showed elevated expressions compared to the control which later at day 7 and day 14 showed downregulation (SI Fig. S3). Similarly, IL-6 showed a significant increase in the expression at day 1 compared to the control, whereas the expression levels ranging from day 3 to day 7 showed day dependent downregulation compared to day 1. Similar results were observed for TGF-β, that is the significant upregulation at day 1 and downregulation from day 3 to day 14 as the wound progresses compared to the control. The angiogenic gene VEGF showed significant increase at day 7 and 14 with non-significant elevation at day 1 and 3 compared to control. The expression of BAX, showed significant upregulation at day 1 and day 3 and later downregulation was observed till day 14, but non-significant compared to control (SI Fig. S3). The COL-1 and MMP-9 showed significant downregulation from day 1 to 3. Additionally, COL-1 also showed significant upregulation at day 14 compared to the control, whereas MMP-9 expression was elevated compared to the other time points and control, but non-significant (SI Fig. S3). The preliminary ANOVA analysis showed a significant induction of IL-1β and IL-6 at days 1 and 3, during acute inflammatory phase of the burn injury process, due to the vital roles of these cytokines in provoking inflammation and attracting immune cells.[13] This was subsequently accompanied with downregulation of the same two cytokines between day 3 and day 14 indicative of the proliferative phase of wound healing. In addition, we found the expression of VEGF was raised significantly on the 7th and 14th day, which might reflect attempts of the body to enhance angiogenesis to repair the tissue.[62] Simultaneously, high expression of the apoptosis related gene BAX implied the on-going cell death, which can hinder the process of tissue regeneration.[63] Early down-regulation of COL-1 and MMP-9 on days 1 and 3 suggested decreased collagen synthesis and degradation, whereas later upregulation of COL-1 on day 14 without any marked change in MMP-9 let into impaired collagen turnover and might induce scar formation in burns not treated.[64]

3.18.2 DPMSCs treated burn wound. The DPMSCs treated burn wound showed significant downregulation in the inflammatory cytokines IL-1β and IL-6. At day 7, significant downregulation was observed in both the expressions of IL-1β and IL-6 compared to the control burn (Fig. 13A). On day 14, significant downregulation was observed up to the baseline, indicating non-significant expression compared to the control. The expression levels of TGF-β were significantly high during the time period of 2 weeks. However, at day 14 the expression was found to be downregulated compared to day 7 (Fig. 13A). VEGF, in contrast showed significant downregulation post treatment compared to the control burn. Further, the apoptotic gene BAX showed significant reduction in the expression post treatment compared to the control burn (Fig. 13A). The remodeling genes, COL-1 and MMP-9 showed significant upregulation at day 7 and at day 14 COL-1 showed significant increase in the treated group, whereas, MMP-9 expression was found to be non-significant (Fig. 13A). Studies have shown that burn animals treated with DPMSCs had lower levels of IL-1β and IL-6 throughout the study period as it helps reduce inflammation which creates a favorable environment for the tissue to regenerate.[65] At both week 7 and 14 the elevated TGF-β levels in DPMSCs treatment assisted in increasing collagen formation and matrix repair to achieve better wound healing with less scar tissue. At day 7 DPMSCs increase COL-1 and MMP-9 production which guides collagen remodeling and helps avoid excessive scarring formation.[66] After 14 days it produced more COL-1 protein and their limited MMP-9 activity likely supports the development of a better collagen structure.

3.18.3 Comparison of blank hydrogel (CHI-PNIPAm) and blank hydrogel seeded with DPMSCs (CHI-PNIPAm/DPMSCs) with control burn. The gene expression of inflammatory cytokines IL-1β showed significant downregulation at day 7 and day 14 in both CHI-PNIPAm (BH) and CHI-PNIPAm/DPMSCs (BHSC) treatment groups compared to the control (Fig. 13B). The IL-6 showed significant downregulation in BHSC and BH treated groups compared to the control at day 7 and 14 (Fig. 13B). In contrast, TGF-β and VEGF, BAX, COL-1 and MMP-9 were found to be significantly downregulated in both the treatment groups compared to the control at both day 7 and 14 (Fig. 13B).

Both the treatment groups BH and BHSC showed better anti-inflammatory effects than those of the control burn, particularly the decrease of IL-1β and IL-6 expressions between day 7 and day14, which was in accordance with the previous studies with hydrogel for burn.[67] Notably, the suppression of IL-1β by BHSC was more suppressed compared to BH alone or DPMSCs alone, suggesting a synergic anti-inflammatory role. Although BH markedly inhibited TGF-β generation, which is related to scar formation, BHSC further promoted wound healing and mitigated scar tissue formation by increasing collagen formation and matrix reconstruction.[68] Curiously, diminished VEGF expression in both BH and BHSC groups were noticed even though DPMSCs are angiogenetic supportive.[69] In addition, both treatment groups significantly reduced BAX gene expression for less cell death and MMP-9. COL-1 was generally inhibited; however, a slight enhancement was observed in BHSC group, which was compared with the standard healing. These results indicate that BH alone has mild anti-inflammatory effects, but the addition of DPMSCs to BHSC increase the therapeutic potential which significantly blocks the most significant post transplantation events of inflammation, collagen expression, and cell survival, being more effectively able to promote healing.

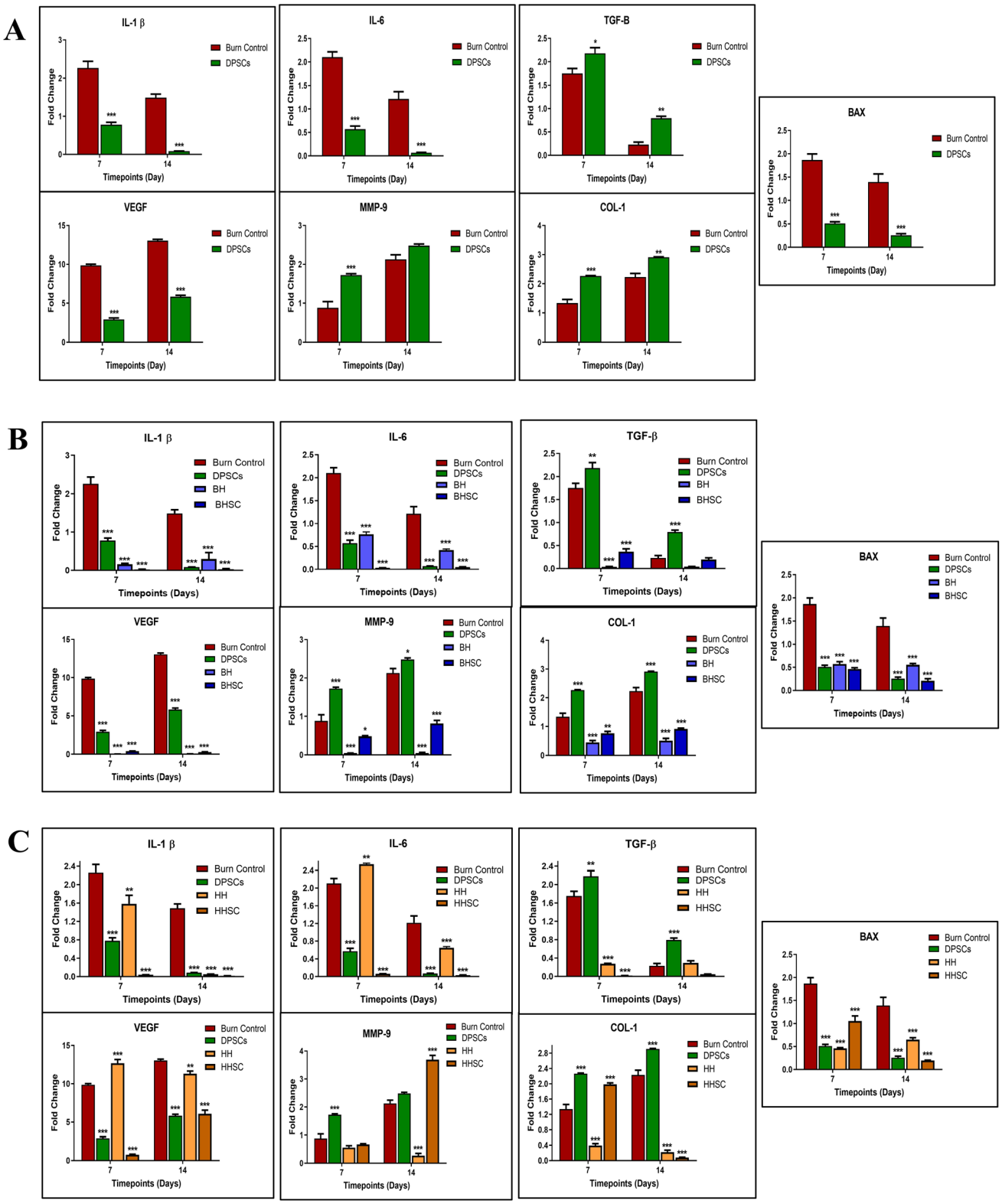

Fig. 13 Gene expression analysis of treated burn wounds. The IL-β, IL-6, VEGF and BAX showed downregulation at both day 7 and 14 compared to control. In contrast, the expressions of TGF-β, COL-1 and MMP-9 were significantly upregulated at both time points compared to control (A). All the genes showed significant downregulation in both the BH and BHSC treated groups at both time points compared to control burn. However, TGF-β, COL-1 and MMP-9 showed significant upregulation in BHSC group compared to BH group, whereas, IL-1β, IL-6 and BAX showed upregulation in BH treated group compared to BHSC group (B). All the genes showed significant downregulation in HHSC treated group compared to control burn at both day 7 and 14, except MMP-9. However, significant upregulation was observed in the expression of IL-1β, IL-6 and VEGF in HH treated group compared to the control group (C). One way ANOVA was used for statistical analysis, followed by Bonferroni's post hoc test and P value of < 0.05 was considered statistically significant (where *** = $p < 0.001$, ** = $p < 0.01$ and * = $p < 0.0$).

3.18.4 Comparison of honey hydrogel (CHI-PNIPAm-HZnO) and honey hydrogel seeded with DPMSCs (CHI-PNIPAm-HZnO/DPMSCs) with control burn. The results showed that the expression of IL-1β was found to be significantly reduced in the CHI-PNIPAm-HZnO/DPMSCs (HHSC) and CHI-PNIPAm-HZnO (HH) treated group both at day 7 and 14, compared to the control (Fig. 13C). In contrast, IL-6 showed similar decrease in the expression of HHSC in 2 weeks of treatment, however significant increase in the expression was observed in the HH treated group at day 7 compared to the control burn (Fig. 13C). The results of TGF-β gene expression were found to be significantly down regulated in both treatment groups at days 7, but a significant increase was observed in the HH group at day 14 compared to the control burn. VEGF expression was significantly higher in HH group but significantly decrease in HHSC group at day 7, whereas, decrease in the expression levels in both treatment groups at day 14 was observed compared to the control burn (Fig. 13C). The expression of BAX was significantly reduced in both the treated groups throughout 2 weeks of time period compared to the control burn. COL-1 showed significant up regulation in the HHSC group and down regulation in the HH group at day 7, however, significant downregulation was observed in both treated groups at day 14 compared to control burn (Fig. 13C). Further, the MMP-9 expression was down regulated in both the treatment groups at day 7, whereas at day 14 the expression level was observed to be significantly increased in the HHSC group and reduced in the HH group compared to the control burn (Fig. 13C).

The effect of HHSC (CHI-PNIPAm-HZnO/DPMSCs) on the wound healing for a period of 2 weeks compared with HH (CHI-PNIPAm-HZnO), showed that the former had more potential to act in the modulation of the healing process. HHSC also significantly decreased the level of IL-1β and IL-6, suggesting suppression of the early inflammation to avoid the formation of chronic wound. Although TGF-β and VEGF are initially suppressed by both treatments at day 7, HHSC was able to more consistently maintain lower levels of these at day 14, which may be indicative of better suppression of scarring and angiogenesis. HHSC also showed a long-term decrease in the apoptotic marker BAX inferring a better protection against cell death. Interestingly, HHSC upregulated COL-1 at day 7 as a stimulant to wound healing in the earlier phase, and subsequently downregulated both COL-1 and MMP-9 by day 14, leading to a more balanced and less visible scar. These results together suggest that HHSC may help in promoting the controlled and effective wound healing.[70] These findings are consistent with the conventional knowledge of the wound healing of honey due to its bacterial, anti-inflammatory, and anti-oxidant attributes.[71] Therefore, it seems that the incorporation of DPMSCs in honey hydrogel could alter these effects by producing an additive effect, as DPMSCs provides a cellular support and enhanced immunomodulatory response while honey might have maintained a protective and nourishing environment, preserving the viability and function of the DPMSCs which can be further evaluated by mechanistic studies including ROS analysis in future.

3.19 Hypermetabolic response evaluation

3.19.1 Hypermetabolic response evaluation of control burn. The hypermetabolic response was evaluated using a full thickness burn model by investigating the levels of corticosterone. It was found to be higher from day 1 onwards till day 21. The levels were found to be significantly increased at day 7 compared to day 1, whereas after day 7 there was a significant time dependent drop observed in the protein expression from day 9 to day 21 compared to day 1 (Fig. 14A). The corticosterone levels significantly rose with the highest level at day 7 (day 9– 21: decline). This initial peak is an immediate response in the activation of the hypothalamic-pituitary-adrenal (HPA) axis to stress, and corticosterone is ultimately a key agent in mobilizing metabolic energy and reducing inflammation. Its reduction in corticosterone levels and changes in thyroid hormone, indicates an adaptation of the body to long-term burn stress and re-establishment of the HPA axis in homeostasis. These results are in agreement with the existing literature on trauma metabolism, indicating the complex interaction of hormonal mediators, and the prolonged recovery time for catabolism and muscle tissue destruction in the context of hypermetabolic response to burn injury.[72,73] Positions of severe burn patients are considered one of the most complex and overwhelming wound injury surface areas sustained by an individual that would affect body functioning. For instance, if 60% or more of TBSA burns are present, a strong reaction termed hypermetabolism occurs, and the acute inflammation that triggers the reaction can basically activate a muscle-mass-extreme motion. This mechanism mobilizes muscle tissue while recovery is incomplete, causing energy demands to surpass energy supply, loss of muscle mass, reduced immune system effectiveness, slow recovery of tissue, and death in the process.[74,75]

3.19.2 Hypermetabolic response evaluation of treated groups. The levels of corticosterone in the DPMSCs, BH, HH and HHSC was significantly lower compared to the control burn, which is almost around 5000 pg mL^{-1} and control burn was more than 6000 pg mL^{-1}. In contrast, the corticosterone levels in BHSC and AHSC were not significantly lower compared to the control burn (Fig. 14B). The corticosterone results showed significantly decreased levels in the DPMSCs and BH group compared to control burn which was found to be slightly lower than these treatment groups. Further, no significant change was observed in the levels of BHSC, HH and HHSC treatment groups compared to the control burn, indicating higher expression levels till the second-week post treatment (Fig. 14C). Hypermetabolism is caused by the release of a plethora of proteins categorized as pro-inflammatory cytokines, or sympatho-neuroendocrine stress-response hormones such as corticosterone, respectively, or a lack of insulin, which can sustain muscle tissue breakdown, a loss of lean body mass, or impair immune responses.[75,76] Managing muscle wasting complications caused by metabolic alterations also delays hospital recovery; thus, tangentially affecting the mortality risk for the patient.[77] Extensive burns have been documented to exert immense tension that in some cases can become life threatening, which leads to a challenging task for clinicians for

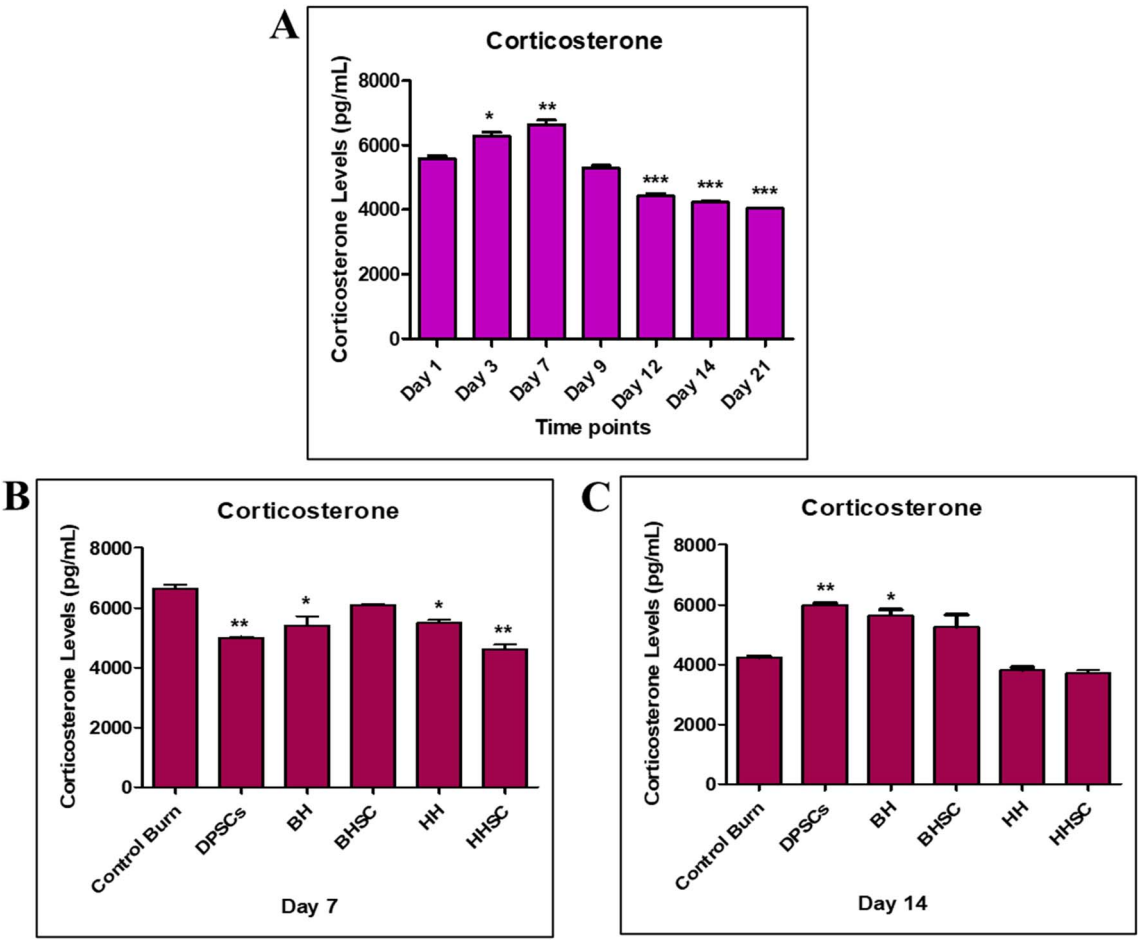

Fig. 14 Protein expression analysis of control burn & treatment groups. The corticosterone levels was significantly increased on day 7 and decrease till day 21 (A). The corticosterone levels were significantly downregulated in all treated groups compared to control (B), whereas, a significant increase in the corticosterone levels were shown in DPMSCs, BH, and AH groups and downregulation was observed in HH and HHSC treated groups on day 14 compared to control (C).

efficient burn management. Our results show diverse impacts of various strategies on the hypermetabolic stress response after burn, based on corticosterone levels. In the beginning of our study (week 1), DPMSCSs, BH, HH, and HHSC-treated mice showed significantly lower corticosterone levels than control burn animals, indicating that these treatments markedly blunted acute stress response and HPA axis activity. But the BHSC did not have this remarkable change, suggesting a distinct pathway or lack of ability to regulate HPA axis. The corticosterone profile (week 2) was elevated and more complicated, in both BH and DPMSCs, being statistically higher than the control burn. The elevated levels in BH and DPMSC is predictably indicative of a continuing or delayed response to stress. On the other hand, BHSC, HH, and HHSC groups did not differ from the control burn on week 2, indicating an underrepresentation of effect on HPA axis activity or a return to baseline. These varied corticosterone responses, in addition to the above-described alterations in inflammatory markers, emphasize the complex and dynamic nature of neuro-endocrine modulation following burn injury and support the different impacts of different treatments on the hypermetabolic response.[78,79] Therefore, comparing the levels of corticosterone on days 7 and 14 post-treatment, it could be appreciated that the various forms of interventional treatments have elicited variable changes in the hypermetabolic response to burn injury. Some of the treatments seem to have an anti-inflammatory effect whereas some may have an influence on the stress reaction and some have none of these impacts. These revelations underscore the importance of understanding the specifics of the processes involved in each treatment to reach the greatest level of use and efficacy in burn patients.

4 Conclusion

The research shows how combining biosynthesized nanoparticles with DPMSCs and a 3D scaffold helps treat severe (scald) burn injuries in rats. The nano-formulated 3D scaffold promoted better wound recovery than a basic scaffold structure by creating a good space for new tissue development. Histological and genetic evaluations show that honey hydrogel support wound healing by reducing inflammation and stimulating collagen growth. Further, by integrating DPMSCs, the treatments

improved as the cells reduced inflammation while increasing collagen levels and lowering rate of cell death. The analysis of the hypermetabolic response of corticosterone showed different results, how each treatment affects the hypermetabolic pathway in severe burn injury. Further, the nanoparticles protected stem cells from the oxidative wound environment, increased their survival, proliferation and migration between cells during tissue regeneration on the 3D scaffold structure.

Therefore, in conclusion, the combination approach of nanoparticles with dental pulp derived stem cells and specialized 3D scaffold shows great promise for potential burn healing. Researchers see this treatment approach as highly valuable for patients with serious burn wounds leading to reduce scarring, skin tissue regeneration and ultimately increased life span.

Future studies can be performed focusing on investigating the long-term safety and efficacy of these biomaterials by performing chronic toxicity studies and efficacy studies in larger animals that better mimic the human skin physiology. Moreover, the clinical translation challenges of scale up manufacturing, development of clinical grade stem cells, immune compatibility and regulatory approval can also be addressed to bring forward this novel strategy closer to reality for therapy in patients with severe burn injuries.

Ethical approval

All experiments involving live subjects were conducted in strict compliance with both international and national guidelines for the care and use of laboratory animals. The study protocols adhered to the principles outlined by the Institutional Animal Care and Use Committee (IACUC, USA), in accordance with the Guide for the Care and Use of Laboratory Animals (National Research Council, 8th edition, 2011), as well as the Institutional Bioethical Committee of the University of Karachi.

The experimental procedures were reviewed and approved by the Institutional Bioethical Committee of the University of Karachi under approval number IBC KU-437/2024. All biosafety and ethical measures were observed throughout the study to ensure animal welfare and humane treatment.

Animals were housed under controlled environmental conditions (temperature, humidity, and light/dark cycle) with unrestricted access to standard food and water. All efforts were made to minimize animal suffering, reduce the number of animals used, and employ alternative methods whenever possible. No unnecessary pain or distress was inflicted, and humane endpoints were strictly followed.

All personnel involved in animal handling, anesthesia, and euthanasia were appropriately trained and conducted procedures in accordance with both IACUC international standards and the Institutional Bioethical Committee's national guidelines.

Conflicts of interest

The authors declare that they have no competing financial or other interests that might influence the publication of this work.

Data availability

Raw data was generated at different departments and institutes in the University of Karachi, Karachi, Pakistan. Derived data supporting the findings of this study are available from the corresponding author Dr Saifullah upon reasonable request.

Supplementary information is available. See DOI: **https://doi.org/10.1039/d5ra06471f**.

References

1 J. Xiong, *Int. J. Mol. Sci.*, 2024, 3100.
2 A. Branski Al-Mousawi, H. Rivero, M. G. Jeschke, A. P. Sanford and D. N. Herndon, *Surg. Infect.*, 2009, 389–397.
3 M. Keck, D. H. Herndon, L. P. Kamolz, M. Frey and M. G. Jeschke, *Wien. Med. Wochenschr.*, 2009, 327–336.
4 R. Kraft, D. N. Herndon, A. M. Al-Mousawi, F. N. Williams, C. C. Finnerty and M. G. Jeschke, *Lancet*, 2012, 1013–1021.
5 F. N. Williams, D. N. Herndon, H. K. Hawkins, J. O. Lee, R. A. Cox, G. A. Kulp and M. G. Jeschke, *Crit. Care*, 2009, 1–7.
6 A. J. Singer, J. W. Zhou, O. B. Osman, Z. B. Harris, M. E. Khani, E. Baer and M. H. Arbab, *Wound Repair Regen.*, 2020, 789–796.
7 M. G. Jeschke, M. E. van Baar, M. A. Choudhry, *et al.*, *Nat. Rev. Dis. Primers*, 2020, **6**, 1–25.
8 M. G. Jeschke, G. G. Gauglitz, G. A. Kulp, C. C. Finnerty, F. N. Williams, R. Kraft, O. E. Suman, R. P. Mlcak and D. N. Herndon, *PLoS One*, 2011, **6**(7), 21245.
9 J. Qin, F. Chen, P. Wu and G. Sun, *Front. Bioeng. Biotechnol.*, 2020, 841583.
10 M. Dominici, K. Le Blanc, I. Mueller, I. Slaper-Cortenbach, F. Marini, D. Krause, R. Deans, A. Keating, D. j Prockop and E. Horwitz, *Cytotherapy*, 2006, **8**, 315–317.
11 X. Wei, X. Yang, Z. P. Han, F. F. Qu, L. Shao and Y. F. Shi, *Acta Pharmacol. Sin.*, 2013, 747–754.
12 Z. Z. Zhang, Y. Hua, K. Yao, L. Liu and Y. Ding, *Am. J. Transl. Res.*, 2018, 3762–3772.
13 I. Khan, S. Aslam, F. Jameel, M. B. Zaidi and A. Salim, *World J. Stem Cell.*, 2020, 1652–1666.
14 M. Wei, S. Li and L. W. Wei, *J. Nanobiotechnol.*, 2017, **15**, 1–13.
15 M. 'Khalid, F. Jameel, T. 'Jabri, A. 'Salim, I. 'Khan and M. R. 'Shah, *RSC Adv.*, 2024, **14**, 28058–28076.
16 J. A. Burdick and G. Vunjak-Novakovic, *Tissue Eng., Part A*, 2009, **15**, 205–219.
17 F. Guilak, D. M. Cohen, B. T. Estes, J. M. Gimble, W. Liedtke and C. S. Chen, *Cell Stem Cell*, 2009, **5**, 17–26.
18 A. Mohamed and M. M. Xing, *Int. J. Burns Trauma*, 2012, **2**, 29.
19 Y. Tian, J. Chen, F. Zahtabi, R. Keijzer and M. Xing, *Pediatr. Pulmonol.*, 2013, **48**, 1098–1111.
20 P. Mohanpuria, N. K. Rana and S. K. Yadav, *J. Nanoparticle Res.*, 2008, **10**, 507–517.
21 J. Lock and H. Liu, *Int. J. Nanomed.*, 2011, **6**, 2769.
22 C. Iancu, I. R. Ilie, C. E. Georgescu, A. R. Biris, T. Mocan and A. S. Biris, *Part. Sci. Technol.*, 2009, **27**, 562–574.

23 A. C. Wan and J. Y. Ying, *Adv. Drug Deliv. Rev.*, 2010, **62**, 731–740.
24 I. Ilie, R. Ilie, T. Mocan, D. Bartos and L. Mocan, *Int. J. Nanomed.*, 2012, **7**, 2211.
25 K. Singh, V. B. Yadav, U. Yadav, G. Nath, A. Srivastava, P. Zamboni, P. Kerkar, P. S. Saxena and A. V. Singh, *Colloids Surf., A*, 2023, **670**, 131575.
26 M. R. Shah, M. Khalid, T. Jabri and S. Ullah, *US Pat.*, 12268698, U.S. Patent and Trademark Office, Washington, DC, 2025.
27 E. Martínez-Sarrà, S. Montori, C. Gil-Recio, R. Nunez-Toldra, D. Costamagna, A. Rotini, M. Atari, A. Luttun and M. Sampaolesi, *Stem Cell Res. Ther.*, 2017, **8**(1), 175.
28 F. N. Williams, D. N. Herndon and M. G. Jeschke, *Clin. Plast. Surg.*, 2009, **36**, 583–596.
29 S. Atapakala, S. S. Sana, B. Kuppam, R. S. Varma, M. A. Aly, S. C. Kim and R. Vadde, *J. Ind. Eng. Chem.*, 2024, **25**, 110–121.
30 M. Sharmila, R. Jothi Mani, A. Kader, A. Ahmad, G. E. Eldesoky, A. E. M. Yahya and A. A. A. Bahajjaj, *Coatings*, 2021, **11**(9), 1046.
31 A. S. Abdelsattar, A. G. Kamel, Y. Elbermawy, H. Gamal and A. El-Shibiny, *Mater. Lett.*, 2024, **15**, 136657.
32 W. M. Argüelles-Monal, J. Lizardi-Mendoza, D. Fernández-Quiroz, M. T. Recillas-Mota and M. Montiel-Herrera, *Polymers*, 2018, **10**, 342.
33 Y. Li, J. Luo, G. Xie, D. Zhu, C. Zhao, X. Zhang, M. Liu, Y. Wu, Y. Guo and W. Yu, *ACS Appl. Polym. Mater.*, 2024, **7**, 1–11.
34 Y. Yuan, K. Raheja, N. B. Milbrandt, S. Beilharz, S. Tene, S. Oshabaheebwa, U. A. Gurkan, A. C. Samia and M. Karayilan, *RSC Appl. Polym.*, 2023, **1**, 158–189.
35 R. Gu, H. Zhou, Z. Zhang, Y. Lv, Y. Pan, Q. Li, C. Shi, Y. Wang and L. Wei, *Nanoscale Adv.*, 2023, **5**, 6017–6037.
36 A. Abdollahi, A. Malek-Khatabi, M. S. Razavi, M. Sheikhi, K. Abbaspour, Z. Rezagholi, A. Atashi, M. Rahimzadegan, M. Sadeghi and H. A. Javar, *J. Drug Deliv. Sci. Technol.*, 2023, **86**, 104627.
37 S. Bharadwaj, B. J. Niebuur, K. Nothdurft, W. Richtering, N. F. van der Vegt and C. M. Papadakis, *Soft Matter*, 2022, **18**, 2884–2909.
38 L. Marsili, M. Dal Bo, F. Berti and G. Toffoli, *Pharmaceutics*, 2021, **13**, 1876.
39 Y. Fan, H. Wang, C. Wang, Y. Xing, S. Liu, L. Feng, X. Zhang and J. Chen, *Polymers*, 2024, **16**, 2818.
40 Y. Yuan, K. Raheja, N. B. Milbrandt, S. Beilharz, S. Tene, S. Oshabaheebwa, U. A. Gurkan, A. C. S. Samia and M. Karayilan, *RSC Appl. Polym.*, 2023, **1**, 158–189.
41 T. Jabri, N. A. Khan, Z. Makhlouf, N. Akbar, J. Gul, M. R. Shah and R. Siddiqui, *Antibiotics*, 2023, **12**, 755.
42 N. Bahari, N. Hashim, K. Abdan, A. Akim, B. Maringgal and L. Al-Shdifat, *Chemosphere*, 2025, **370**, 143961.
43 W. Y. Dong Q, F. Mohabatpour, L. Zheng, S. Papagerakis, D. Chen and P. Papagerakis, *Methods Mol. Biol.*, 2019, 91–101.
44 M. Honda and H. Ohshima, *J. Oral Biosci.*, 2022, 26–36.
45 C. L. Stewart, A. L. Hook, M. Zelzer, M. Marlow and A. M. Piccinini, *Cell Biochem. Funct.*, 2024, 4097.
46 H. Cao Duan L, Y. Zhang, J. Cao and K. Zhang, *Signal Transduct. Targeted Ther.*, 2021, 1–31.
47 K. Mitchell, S. S. Panicker, C. L. A. G. Adler and K. R. Hixon, *Gels*, 2023, 877.
48 R. F. El-Kased, R. I. Amer, D. Attia and M. M. Elmazar, *Sci. Rep.*, 2017, 9692.
49 G. F. Caetano, M. A. C. Frade, T. A. M. Andrade, M. N. de Leite, C. Z. Bueno, Â. M. Moraes and J. T. Ribeiro-Paes, *J. Biomed. Mater. Res. B Appl. Biomater.*, 2014, 10–13.
50 L. F. Gushiken, C. A. Hussni, J. K. Bastos, A. L. Rozza, F. P. Beserra, A. J. Vieira, C. R. Padovani, M. Lemos, M. P. Junior, J. J. Silva and R. H. Nóbrega, *Environment*, 2017, **23**, 2.
51 P. Zhao Zhang Y, X. Chen, C. Xu, J. Guo, M. Deng, X. Qu, P. Huang, Z. Feng and J. Zhang, *Adv. Sci.*, 2023, **10**(11), 2206585.
52 G. Sazegar, A. H. Seyed Reza and E. Behravan, *Iran. J. Basic Med. Sci.Iran J Basic Med Sci*, 2011, **14**, 391–398.
53 S. Abolhassani, H. Alipour, A. Alizadeh, M. Mehdi Nemati, H. Najafi and O. Alavi, *J. Ind. Textil.*, 2022, **51**, 954S–968S.
54 Z. Lateef, G. Stuart, N. Jones, A. Mercer, S. Fleming and L. Wise, *Int. J. Mol. Sci.*, 2019, **20**, 538.
55 O. B. Hamida, M. K. Kim, Y. K. Sung, M. K. Kim and M. H. Kwack, *Cells*, 2025, **14**, 7.
56 Z. Mbese, S. Alven and B. A. Aderibigbe, *Polymers*, 2021, **13**, 4368.
57 M. Mardani, A. Sadeghzadeh, N. Tanideh, A. Andisheh-Tadbir, F. Lavaee, M. Zarei and J. Moayedi, *DOAJ*, 2020, 1618.
58 J. Y. Ren, S. Y. Zhang and B. Yang, *World J. Stem Cell.*, 2021, 1625–1646.
59 H. Guo, R. A. Hamid, R. M. Ali, S. K. Chang, M. H. Rahman, Z. Zainal and H. Khaza'ai, *Antioxidants*, 2020, 130.
60 J. Yupanqui Mieles, C. Vyas, E. Aslan, G. Humphreys, C. Diver and P. Bartolo, *Pharmaceutics*, 2022, **14**, 1663.
61 S. A. Abraham, G. Yashavanth, R. Deveswaran, S. Bharath, M. Azamathulla and S. Shanmuganathan, *Mater. Today Proc.*, 2022, **49**, 1709–1718.
62 L. Kuang Huang J, Y. Liu, X. Li, Y. Yuan and C. Liu, *Adv. Funct. Mater.*
63 H. Kubo, T. Hayashi, K. Ago, M. Ago, T. Kanekura and M. Ogata, *Leg. Med.*, 2014, **16**, 8–13.
64 A. A. Mamun, C. Shao, P. Geng, S. Wang and J. Xiao, *Front. Immunol.*, **24AD**(15), 1395479.
65 P. Prateeksha, S. Anderson and H. Das, *Biomedicines*.
66 H. J. Sung, C. E. Johnson, S. M. Lessner, R. Magid, D. N. Drury and Z. S. Galis, *Tissue Eng.*, 2005, 267–276.
67 W. Zhong, H. Meng, L. Ma, X. Wan, S. Chen, K. Ma and C. Zhang, *View*, 2024, **5**, 20230110.
68 X. Lin and Y. Lai, *Int. J. Mol. Sci.*, 2024, **25**, 1458.
69 M. Shekatkar, S. Kheur, S. Deshpande, A. Sanap, A. Kharat, S. Navalakha, A. Gupta, M. Kheur, R. Bhonde and Y. P. Merchant, *Eur. J. Paediatr. Dent.*, **18**, 712–742.
70 N. Navaei-Alipour, M. Mastali, G. A. Ferns, M. Saberi-Karimian and M. Ghayour-Mobarhan, *Phytother Res.*, 2021, 3690–3701.
71 B. Nikahval, N. Naderi, E. Abedi, M. Jafari, B. Nikahval, N. Naderi and M. Jafari, *J. Clin. Diagn. Res.*, 2020, **1–5**.

72 A. Clark, J. Imran, T. Madni and S. E. Wolf, *Int. J. Burns Trauma*, 2017, **5**, 11.
73 C. B. Nielson, N. C. Duethman, J. M. Howard, M. Moncure and J. G. Wood, *J. Burn Care Res.*, 2017, **38**, e469–e481.
74 D. N. Herndon and R. G. Tompkins, *Lancet*, 2004, **363**, 1895–1902.
75 T. L. Palmieri, S. Levine, N. Schonfeld-Warden, M. S. O'Mara and D. G. Greenhalgh, *J. Burn Care Res.*, 2006, **27**, 742–748.
76 M. G. Jeschke, D. L. Chinkes, C. C. Finnerty, G. Kulp, O. E. Suman, W. B. Norbury, L. K. Branski, G. G. Gauglitz, R. P. Mlcak and D. N. Herndon, *Ann. Surg.*, 2008, **248**, 387–401.
77 C. Pereira, K. Murphy, M. Jeschke and D. N. Herndon, *Int. J. Biochem. Cell Biol.*, 2005, **37**, 1948–1961.
78 B. E. Leonard and A.-M. Myint, *Acta Neuropsychiatr.*, 2009, **45**.
79 H. Zhang, M. Wang, X. Zhao, Y. Wang, X. Chen and J. Su, *Brain Behav. Immun.*, 2024, **116**, 286–302.